

Attention to Quantum Complexity

Hyejin Kim^{†,1}, Yiqing Zhou^{†,1}, Yichen Xu^{†,1}, Kaarthik Varma,¹ Amir H. Karamlou,²
Ilan T. Rosen,³ Jesse C. Hoke,^{4,5} Chao Wan,⁶ Jin Peng Zhou,⁶ William D.
Oliver,^{2,3,7} Yuri D. Lensky,^{1,4} Kilian Q. Weinberger,⁶ and Eun-Ah Kim^{1,4,8,*}

¹*Department of Physics, Cornell University, Ithaca, NY, USA*

²*Department of Physics, Massachusetts Institute of Technology, Cambridge, MA 02139, USA*

³*Research Laboratory of Electronics, Massachusetts Institute of Technology, Cambridge, MA 02139, USA*

⁴*Google Research, Mountain View, CA, USA*

⁵*Department of Physics, Stanford University, Stanford, CA, USA*

⁶*Department of Computer Science, Cornell University, Ithaca, New York 14853, USA*

⁷*Department of Electrical Engineering and Computer Science,
Massachusetts Institute of Technology, Cambridge, MA 02139, USA*

⁸*Department of Physics, Ewha Womans University, Seoul, South Korea*

[†]*These authors contributed equally to this work.*

The imminent era of error-corrected quantum computing urgently demands robust methods to characterize the relative complexity of quantum states, even from limited and noisy measurements. We introduce the Quantum Attention Network (QuAN), a versatile, classical AI framework leveraging the power of attention mechanisms specifically tailored to address the unique challenges of learning quantum complexity. Inspired by large language models, QuAN treats measurement snapshots as tokens while respecting their permutation invariance. Combined with a novel parameter-efficient mini-set self-attention block (MSSAB), such data structure enables QuAN to access high-order moments of the bitstring distribution and preferentially attend to less noisy snapshots. We rigorously test QuAN across three distinct quantum simulation settings: driven hard-core Bose-Hubbard model, random quantum circuits, and the toric code under coherent and incoherent noise. QuAN directly learns entanglement and state complexity growth from experimentally obtained computational basis measurements. In particular, it learns the growth in complexity of random circuit data upon increasing depth from noisy experimental data. Taken to a regime inaccessible by existing theory, QuAN unveils the complete phase diagram for noisy toric code data as a function of both noise types. This breakthrough highlights the transformative potential of using purposefully designed AI-driven solutions to assist quantum hardware.

Artificial intelligence (AI) and quantum information science are among the most active areas in cutting-edge science and technology, addressing the computational complexity frontier. Although these two domains have evolved separately in the past, recent breakthroughs in both fields create a unique opportunity to employ AI to learn quantum complexity. The most paradigm-shifting aspect of the latest large language models, such as ChatGPT, is their generality: generally trained big models can reason in many different complex settings using natural languages. As quantum hardware platforms enter a new era with error correction within reach [1–3], a new general-purpose method for deciphering quantum states with unprecedented levels of complexity and entanglement is critically needed. We ask a compelling question: Can the core mechanism of the success of the large language models, the attention mechanism [4, 5], drive a general-purpose machine for learning quantum complexity? The answer to this question will hinge upon whether an intelligent use of the attention mechanism can hit the core aspects of the quantum complexity using only a polynomial in system size number of measurements from noisy devices.

Quantum complexity, once an abstract information theoretical concept, has become a lynchpin at the intersection of multiple subfields: the study of black holes and geometric theory of wormholes[6–8], quantum information[9–11], topological states [12–14], and thermalization studies [15–20]. Relative complexity between two states represented by density matrices ρ_α and ρ_β aims to quantify the difficulty of producing one from the other. For pure states $|\alpha\rangle$ and $|\beta\rangle$ Brown and Susskind [7] defined it in terms of circuit complexity, i.e., the minimal number of gates required to implement a unitary U connecting the states ($|\beta\rangle = U|\alpha\rangle$). Although helpful in exploring quantum chaos, directly applying the definition by computing an efficient circuit is often impractical. The challenge is further aggravated by the fact that experimental systems are invariably in mixed states. Theoretical extensions like purification complexity [21] and complexity entropy [22] demand additional quantum computations, complicating practical use. In practice, our knowledge of states ρ_α and ρ_β is limited to the collection of their measurement bitstring outcomes, $\{B_j\}_\alpha$ and $\{B_j\}_\beta$, and the operations done to the states just before measurements (see Figure 1(a)). From a data-centric point of view, the task of learning the relative complexity between ρ_α and ρ_β from available data is a

* Corresponding author: eun-ah.kim@cornell.edu

binary classification task of distinguishing

$$\{B_j\}_\alpha \text{ v.s. } \{B_j\}_\beta, \quad (1)$$

where $j = 1, \dots, M$, with the sample size M .

Expectation values of observables, such as order parameters, are the most common and classic choice for comparing two states ρ_α and ρ_β . Even when the observable is not known apriori, discovering characteristic spatial motifs using machine learning has been powerful when the two states can be distinguished by quantities linear in density matrices [23–29]. At the opposite extreme of ambition for learning to characterize a state ρ is to model the full probability distribution of bit strings associated with the given state ρ in the space of 2^{N_q} possibilities

$$p(\{b_i\}|\rho), \quad i = 1, \dots, 2^{N_q}, \quad (2)$$

where N_q is the number of qubits, from the measurement data $\{B_j\}$. While the advantage of generative modeling has been explored [30–35], such modeling is ultimately restricted to relatively small systems. A natural middle ground would be to learn key features of the probability distribution in Eq. 2 through moments of the distribution. This approach can be motivated both from a purely statistical perspective and from the perspective of the analysis of local chaotic dynamics’ approach to purely random evolution[15, 36, 37].

Here, we introduce the Quantum Attention Network (QuAN) shown in Fig. 1(b) as a general-purpose AI for learning relative quantum complexity between two states ρ_α and ρ_β through binary classification between the measurement bitstrings $\{B_j\}_\alpha$ and $\{B_j\}_\beta$. The QuAN capitalizes on the fact that the self-attention mechanism [4] learns the varying significance of the correlation between words at arbitrary distances within a sentence. However, while words in a sentence form a sequence, the order of bitstrings generated by identical experiments has no meaning. Through multiple layers of self-attention blocks attending between bitstrings in a manner that is manifestly permutation invariant, the QuAN approximately learns high moments of the distribution $p(\{b_i\}|\rho)$ from a finite number of samples (see SM section A for more detail). Furthermore, by attending to snapshots less affected by noise, the QuAN extracts target features of pure state in the presence of a finite amount of noise. In the rest of the paper, we present the design principles of the QuAN guided by the learning goals and demonstrate the QuAN’s efficacy as a general-purpose AI by deploying QuAN to learn relative complexity between two states ρ_α and ρ_β that differ in ways that are fundamental to three frontiers: entanglement transition, chaotic dynamics, and error correction, as sketched in Fig. 1(c-e).

Fig. 1(b) shows the QuAN architecture and the data flow through QuAN. QuAN takes a set of snapshots \mathbf{X}_i as input and outputs the machine’s confidence $y(\mathbf{X}_i) \in [0, 1)$ on the input belonging to class α between the binary choice of α and β . To attend between snapshots, we first

partition the complete data consisting of M snapshots into sets consisting of N snapshots. Typically, we train with 70 ~ 75% of data and validate with the rest (see SM section C2, D2, E2 for more detail). Each set \mathbf{X}_i then goes through three stages in sequence: convolution, encoder, and decoder stage (see Fig. 1(b)). The convolution stage incorporates local spatial features and maps the binary-valued \mathbf{X}_i to vectors \mathbf{x}_i with continuous entries with better algebraic properties for sampling moments. In language models, the encoding stage transforms the input into an informative, learned representation. For QuAN’s encoding to target moments of \mathbf{x}_i , we introduce Mini-Set Self-Attention Blocks (MSSABs). Unique to the QuAN architecture, MSSAB is adapted from a permutation-invariant version of the transformer [38] to access high moments of the distribution in a parameter-efficient manner. It accesses up to $2N_s^2$ order correlations for N_s mini-sets within one layer.

The decoder stage consists of the pooling attention block (PAB) and the single-layer perceptron that compresses all the information into the confidence output(see SM section A4). The PAB layer learns to attend more to the snapshots with features characteristic of the target state. When the confidence is $y(\mathbf{X}_i) < 0.5$, QuAN assesses the data to belong to state α ; otherwise, it is assessing the data to belong to state β . We train QuAN by minimizing binary cross entropy loss between the ground truth and QuAN’s prediction through Adam optimization. The multi-faceted use of attention mechanisms empowers QuAN to be a versatile general-purpose AI capable of learning quantum complexity in various datasets.

First, we consider the relative complexity between states with different entanglement scaling: a volume-law scaling state and an area-law scaling state (see Fig. 1(c)). The distinction is significant because classical computers cannot efficiently represent a general volume-law scaling state. Moreover, the change in entanglement scaling signals measurement-induced phase transitions [39–44]. Nevertheless, extraction of the entanglement scaling is often challenging since it requires randomized multi-basis measurements or state tomography for subsystems with varying sizes [45]. Our key insight is that QuAN can learn the change in the entanglement scaling by attending between snapshots within the set (see Fig. 2(a)). The self-attention score for the set \mathbf{X}_i in each self-attention block (SAB) is given by

$$\langle Q_{\mathbf{x}_i} | K_{\mathbf{x}_i} \rangle = (Q_{\mathbf{x}_i})(K_{\mathbf{x}_i})^T \quad (3)$$

up to normalization, where \mathbf{x}_i is convolved from the snapshot set \mathbf{X}_i as shown in Fig. 1(b); Q, K are two trainable transformation matrices, often referred to as query (Q) and key (K) (See SM section A3a for more detail.). When two Z -basis snapshots are related by simultaneous bit-flips at a pair of qubits (j, k), the attention score reflects the correlation $\langle X_j X_k \rangle$ which is upper-bounded by their mutual information [46] (see Fig. 2(a) and also SM section C5). Hence, QuAN can access Pauli X correlations from Z -basis measurement through inter-snapshot

attention. In an area-law state, a X correlation is concentrated between nearby qubits. On the other hand, in a volume-law state, the entanglement of each qubit shared with the entire system dilutes the X correlation. By accessing the X correlation through inter-snapshot attentions, QuAN may witness the entanglement transition from just Z -basis snapshots.

To verify QuAN's potential for witnessing the entanglement transition from the Z -basis measurements, we turn to coherent-like states prepared to be superposition of hard-core Bose Hubbard model energy eigenstates reached through a driven Hamiltonian

$$H/\hbar = \sum_{\langle j,k \rangle} J_{jk} \hat{\sigma}_j^+ \hat{\sigma}_k^- + \frac{\delta}{2} \sum_j \hat{\sigma}_j^z + \Omega \sum_j (\alpha_j \hat{\sigma}_j^- + \text{h.c.}), \quad (4)$$

implemented using a superconducting, transmon-based quantum simulator (see Fig. 2(b)). Here, $\hat{\sigma}_j^+$ ($\hat{\sigma}_j^-$) represents the raising (lowering) operator on qubit at site j and $\hat{\sigma}_j^z$ represents the Pauli Z operator at site j ; J_{jk} is the particle exchange interaction strength between site j and k of average value J , δ is the detuning between the drive and qubit frequency, and Ω is the drive strength (see SM section C1). Upon tuning δ/J , the system prepares a coherent-like superposition of states at the center of the spectrum for small δ/J and that of states at the edge of the spectrum for large δ/J [45]. Bipartite entanglement entropy calculated from subsystem tomography using subsystem measurements in an informationally complete basis set found the volume law scaling at low values of $|\delta|/J$ the area law scaling at large values of $|\delta|/J$ (see Fig. 2(c)). Here, we use the experimental snapshots of the entire system in the particle number basis, which maps to Z -basis measurements in the hard-core limit over a range of δ/J .

To investigate QuAN's capability and the role of *attention* in witnessing the entanglement transition, we compared the performance of three different architectures with varying degrees of *attention*. The simplest architecture is the Set MultiLayer Perceptron (SMLP) without the self and pooling attention blocks (see Fig. 2(d)). The SMLP is a generalization of the usual multilayer perception [47] designed to take a set of snapshots as input and learn the positional information through convolution. We set the mini-set size for the other two architectures to $N_s = 1$, which reduces the MSSAB to a single SAB. QuAN₂ and QuAN₄ each access up to the 2nd and 4th moments through SAB layers (see SM section A3d).

The task for the three architectures is to witness the change in the entanglement scaling upon increase in δ/J by training the models to distinguish the $\delta/J = 0$ state from the $\delta/J = 2$ state using snapshots with the same number ($n = 8$, see SM section C2) of bosons. All three architectures were trained and tested using $M = 69632$ experimental snapshots from $\delta/J = 0$ and the same number of snapshots from $\delta/J = \pm 2$ with the binary label: $y = 1$ for data from $\delta/J = 0$ with volume-law entanglement and $y = 0$ for data from $\delta/J = \pm 2$ with area-law

entanglement.

Fig. 2(e-g) compares the performance of the three architectures based on 10 independent trainings for each architecture. When an architecture learns to witness the entanglement transition, average confidence $\bar{y} = \langle y(\mathbf{X}_i) \rangle_i$ should span between $\bar{y} = 1$ at $\delta/J = 0$ and $\bar{y} = 0$ at $\delta/J = 2$ (see SM section C3). Fig. 2(e) shows SMLP fails to learn the entanglement transition, given the average confidence remaining flat at $\bar{y} = 0.5$ independent of set size N (see Fig. 2(e)). By contrast, QuAN₂, which only uses second moments of bit strings, already learns the entanglement transition once a set structure is used. Moreover, its learning improves with increasing set size within the bounds of the total sample size (see Fig. 2(f) and see SM section C4). Accessing up to the fourth moment, QuAN₄ shows sharper transition with reduced error bars across different training. The above comparison showcases the QuAN's ability to witness changes in entanglement scaling using Z -basis measurements alone through inter-snapshot attention.

Next, we move on to learning the relative state complexity between shallow and deep random circuit states: ρ_{shallow} v.s. ρ_{deep} . The random circuits have become a theoretical paradigm for studying diverse sets of phenomena in quantum dynamics from information processing in black holes [48] to quantum chaos and thermalization [15, 49–51]. Despite being composed of local gates (see Fig 3(a)), the ensemble of random circuits accurately approximates the ensemble of global random unitary transformations up to the first k -moments, where k grows with the depth of the circuit [36]. Furthermore, Ref. [15] established that such random circuits' complexity would grow linearly with k . We aim to learn the evolution of state complexity in random circuits as a function of depth by employing QuAN for multiple pairwise classification tasks that contrast data from variable depth d with data from $d = 20$. Training QuAN to perform this classification probes its ability to learn higher-order features of the bit-string data, like aspects of the third and higher moments of the bit-string distribution [15], that reflect the relative complexity of the state at depth d compared to the state at depth $d = 20$. We anticipate such relative complexity will shrink with increasing depth d . To coalesce QuAN's learning across different training runs for each depth, we study the classification accuracy defined as the percentage of correctly classified inputs [52].

While previous experiments primarily focused on deep circuits pushing against the limits of classical simulation, we systematically explore the increase in complexity as depth increases. We consider both experimental data from quantum hardware (see SM section D1 for experimental details) and data from the corresponding pure state implemented on classical hardware. At each circuit depth d , we sample $N_c = 50$ random circuit instances. For each circuit instance, we collect $M_s = M/N_c = 500,000$ bit-strings ($M_s = 2,000,000$ for $N_q = 36$). To prevent QuAN from over-fitting a spe-

cific circuit instance, we train QuAN using data from 70% of all the circuit instances and reserve the remaining 30% circuits for testing (see SM section D2.) We batch bitstrings fbitstrings circuit instance into sets of N bit-strings, bitstrings as shown in Fig. 3(b). See SM Section D3 for more details on training and testing.

We benchmark the QuAN’s learning of relative complexity at each circuit depth d against the depth dependence of the linear cross entropy benchmark (XEB). The linear XEB, \mathcal{F}_{XEB} , for a collection of bit-strings $\{B_j\}$ is defined by

$$\mathcal{F}_{\text{XEB}}[\{B_j\}] = 2^{N_q} \langle p_U(B_j) \rangle_j - 1, \quad (5)$$

where $p_U(B_j)$ is the probability for the given bit-string B_j to be sampled from an ideal pure state $U|0\rangle^{\otimes N_q}$ for the random unitary circuit U of depth d (see SM section D1b for detail). We first study the depth-dependent relative complexity of the ideal pure-state data. When $\{B_j\}$ is sampled from the same ideal pure state, $\mathcal{F}_{\text{XEB}}[\{B_j\}]$ measures the second moment of the bit-string dbitstring associated with the pure state. As shown in Fig. 3(c), the XEB for such bit-string cbitstrings saturates the infinite depth asymptotic value of $\mathcal{F}_{\text{XEB}} = 1$ to polynomial precision near depth $d = 8$ for all system sizes considered, becoming blind to circuit dynamics past $d = 8$. The relative complexity learned by QuAN quantified through classification accuracy shrinks upon increasing depth as expected, approaching the vanishing relative complexity at 50% accuracy of the classification task. Nevertheless, remarkably, QuAN₅₀ that accesses upto 50th moments (see SM section A3) learns the relative complexity of $d = 8$ for all system sizes (see Fig. 3(d)). Furthermore, the classification accuracy at $d = 8$ shows promising sub-exponential scaling with the increase in the system size (see SM section D4 for more detail.)

Comparing various architectures’ learning of relative complexity at depth $d = 8$ shown in Fig. 3(e) reveals how difficult this task is for most architectures. Despite all having the same number of hyper-parameters, architectures other than QuAN failed to learn the relative complexity of $d = 8$ and 20. Notably, the failure of three architectures that took individual bit-strings bitstring without forming a set structure (the MLP, the convolutional neural network (CNN), and the standard transformer (Transf.), see SM section B) establishes the importance of the set structure for learning relative complexity. The failure of the SMLP and pooling attention block (PAB) shows that using a set structure is not enough without self-attention. With just a single layer of MSSAB, QuAN learns the relative complexity of depth $d = 8$ (QuAN₂ in Fig. 3(e)). Allowed to learn up to 50th moment, QuAN₅₀’s accuracy shoots up to demonstrate the benefit of MSSAB accessing higher moments. In the rest of the paper, we focus on the performance of QuAN₅₀ with a single MSSAB block ($L = 1$) containing $N_s = 5$ mini-sets.

The advantage of QuAN’s relative complexity learning is further pronounced when the bit-strings bitstrings ,

$\{B_j\}$, are experimentally sampled. For such data, the XEB $\mathcal{F}_{\text{XEB}}[\{B_j\}]$ estimates the correspondence between experimental snapshots and the snapshot distribution of the ideal circuit up to second order. As shown in Fig. 3(f), $\mathcal{F}_{\text{XEB}}[\{B_j\}]$ for the experimental data smoothly evolves to 0, reflecting the increase in noise with increasing depth which pushes the system closer to the maximally mixed state rather than the intended pure state. Dominated by the noise, \mathcal{F}_{XEB} on experimental data does not reveal the increase in complexity driven by the intended unitary evolution. QuAN also confirms the significant influence of increasing noise when the depth-dependence of relative complexity is probed by training and testing QuAN entirely on experimental data (see SM section D). The key question is whether learning the remnants of the pure state dynamics from noisy experimental data is possible.

One way to learn the aspect of relative complexity that corresponds to pure state dynamics from the experimental data is to quantify the relative complexity of experimental bit strings using QuAN trained on noiseless pure state data. Surprisingly, the depth-dependence of the pure-state-trained QuAN’s classification accuracy of experimental data in Fig. 3(g) shows a trend that closely follows corresponding depth-dependence in its inspection of the noiseless simulated data shown in Fig. 3(d). Specifically, both exhibit a transition at depth $d = 10$. Hence, QuAN was able to reveal traces of pure-state complexity evolution from noisy experimental data.

Overcoming noise in relative complexity learning is particularly important for noisy states from error-correcting codes. As the quantum hardware approaches the breakeven point, the community is increasingly focused on learning topological order, a phase of matter which supports quantum error-correction, in a mixed state [12, 53–57]. Earlier literature on the complexity of topological states focused on the relative complexity of topological states compared to a simple product state $|0\rangle^{\otimes N_q}$. It is known that topological states’ relative complexity with respect to $|0\rangle^{\otimes N_q}$ grows linearly with the system size. However, much less is known about the relative complexity between a topological state and an undecodably noised state.

One leading candidate for fault-tolerant quantum memory is the toric code or \mathbb{Z}_2 topological order. In its ideal ground state |TC> a closed Z -loop operator around a loop γ , $Z_{\text{closed}}(\gamma) \equiv \prod_{i \in \gamma} Z_i$, has length-independent expectation value

$$\langle \text{TC} | Z_{\text{closed}}(\gamma) | \text{TC} \rangle = 1. \quad (6)$$

Infinitesimal noise introduces tension to the above loop operator expectation value, resulting in its exponential decay with the loop perimeter [58], as it is illustrated in Fig. 1(e) for incoherent noise. Hence any amount of noise destroys topological order from the loop tension perspective. Nevertheless, mapping the limiting cases to statistical mechanics models reveals hidden phase transitions. Specifically, with just the coherent noise g_X mod-

eled through

$$|\Psi(g_X)\rangle = \frac{1}{\sqrt{\mathcal{N}}} \exp\left(g_X \sum_i X_i\right) |\text{TC}\rangle, \quad (7)$$

where \mathcal{N} is a normalization factor, the error threshold of $g_X \approx 0.22$ was established in Ref. [59] via mapping the problem to a classical 2D Ising model. Alternatively, with just an incoherent noise p_{flip} modeled through bit-flip error channel

$$\mathcal{E}_i(\rho) = (1 - p_{\text{flip}})\rho + p_{\text{flip}}X_i\rho X_i, \quad (8)$$

for each qubit i , error threshold of $p_{\text{flip}} \approx 0.11$ was established in Ref. [53] via mapping the error model to the random bond Ising model [60]. However, the phase diagram interpolating between the two axis is yet to be achieved. Motivated by QuAN’s successes, we employ QuAN to solve this open problem.

To study the effect of coherent and incoherent noises in a controlled way, we use classically simulated toric code ground state modified by coherent noise strength g_X , available at [61] as a part of Ref. [62]. To the Z -basis bit-string d bitstringd from this state, we implement the error channel Eq. 8 through random bitflips (see SM section E1). We then transform the resulting bit-strings bitstringsements of the smallest loops, building on the insight of Ref. [28]. Now, the collection of these plaquette values goes into QuAN as input. To arrive at QuAN that interpolates between the two axis of the noise phase space (g_X, p_{flip}) in its learning of the relative complexity between decodable and undecodable states, we train QuAN with nearly coherent data over the range of g_X value and deeply incoherent data over the same range of g_X value (see Fig. 4(c,d) and SM section E2). We then classify the data from the rest of the phase space.

Fig. 4(c,d) shows that with sufficiently large set-size, QuAN confidence marks a sharp distinction between decodable and undecodable states, saturating the error threshold for incoherent noise $p_{\text{flip}} \approx 0.11$. The cut along the $g_X = 0$ axis Fig. 4(e) shows that set structure and the attention mechanisms in QuAN are essential. Upon increasing the set size, the transition is sharpening towards $p_{\text{flip}} \approx 0.11$ along $g_X = 0$ axis. Remarkably, with the set size of $N = 64$, the QuAN observes a sharp transition close to the theoretically predicted coherent noise threshold of $g_X \approx 0.22$ along the $p_{\text{flip}} = 0$ axis [63](see Fig. 4(f)). This is surprising given that we did not explicitly train QuAN to contrast $g_X = 0$ vs large $g_X \neq 0$ and warrants further theoretical investigation into the potential existence of a unifying statistical mechanics model.

The model ablation studies (see Fig. 4(g,h) and SM section E4) revealed the critical role of the pooling attention decoder as an automatic importance sampler with excellent sample complexity. Specifically, we tried removing the self-attention stage entirely, leaving only the pooling attention stage; we refer to the resulting architecture as PAB. When comparing the average confidence of the PAB architecture shown in Fig. 4(g,h) with

that of QuAN₂, we observe that PAB effectively saturates the known thresholds along both axes, for set size $N = 64$. This allows in-depth interpretation of the machine’s learning since the pooling attention score of the PAB can be traced to individual snapshots \mathbf{X}_i (see SM section E5).

By comparing the snapshots with high and low pooling attention scores, we can gain insight into the feature of the data recognized as that of a topological phase. For this, we inspect the distribution of the pooling attention score across all the snapshots with $p_{\text{flip}} = 0.05$ and $g_X = 0$ shown in Fig. 4(i). Selecting the snapshots with top 15% and bottom 15% of the distribution, we analyze the subset average value of the Z -loop operator Z_{closed} for a closed loop γ as a function of the length of the perimeter (see Fig. 4(j) [64].) The contrast in the length dependence of the loop expectation value $\langle Z_{\text{closed}} \rangle$ between the high and low attention groups is striking. The snapshots in the high attention score group show large $\langle Z_{\text{closed}} \rangle$ with weak perimeter length dependence until the length hits the system size. On the other hand, for the snapshots in the low attention score group $\langle Z_{\text{closed}} \rangle$ decays immediately after the smallest loop perimeter. Hence, it appears QuAN learned to selectively attend to snapshots with vanishing loop tension. QuAN’s importance sampling is a data-efficient alternative to seeking a dressed loop operator [58, 62] with a length-independent expectation value or information-theoretical measures [12, 55, 59]

To summarize, we introduced QuAN, a versatile general-purpose architecture that adopts the attention mechanism for learning relative quantum complexity between two states. QuAN is built on three principles: (1) treat the snapshots as a set with permutation invariance, (2) attend between snapshots to access higher moments of bit-string d bitstringn, and (3) attend over snapshots to importance sample. QuAN treats each snapshot as a “token” and leverages the capability of stacked L -layers of N_s mini-set self-attention to sample $(2N_s^2)^L$ -th moments of snapshots. We put QuAN to work on three challenging sets of Z -basis data to showcase the power of QuAN and gain new insights. With the driven hard-core Bose-Hubbard model data, we discovered that the entanglement transition between the volume-law and area-law scaling regimes can be witnessed entirely with the Z -basis measurements. With random circuit sampling data, we revealed the evolution of complexity with increasing depth from noisy experimental data that reflects noise-free evolution. Finally, with the mixed state data of toric code with coherent and incoherent noise, we obtained the first decodability phase diagram that saturates known error thresholds. QuAN’s discoveries set new challenges for theoretical understanding. Simultaneously, QuAN’s ability to learn relative quantum complexity through the adaptive use of attention mechanisms holds promise for quantum error correction, the key data-centric problem for the application of quantum hardware. While an AI’s learning is typically hard to interpret, we revealed the critical role of self-attention and pulling at-

tion through ablation studies. Promising future directions for the application of QuAN include the development of a decoder for quantum error correction codes and learning measurement-induced phase transitions.

Data availability. The data are available upon reasonable request.

Code availability. All codes used for training and data analysis of the QuAN are available at Github, https://github.com/KimGroup/QuAN_code.

Acknowledgements. We thank Juan Carrasquilla, Sarang Gopalakrishnan, Tarun Grover, Robert Huang, John Preskill, Nick Read, and Pedram Roushan for helpful discussions. We thank Iris Cong, Nishad Maskara, and Misha Lukin for sharing the toric code simulation data prior to publication and for discussions. HK, YX, KV, YL, CW, JZ, KQW, and E-AK acknowledge support from the NSF through OAC-2118310. YZ acknowledges support from NSF Materials Research Science and Engineering Center (MRSEC) through DMR-1719875 and from Platform for the Accelerated Realization, Analysis, and Discovery of Interface Materials (PARADIM), supported by the NSF under Cooperative Agreement No. DMR-2039380. ITR is supported by an appointment to the Intelligence Community Postdoctoral Research Fellowship Program at the Massachusetts Institute of Technology administered by Oak Ridge Institute for Science and Education (ORISE) through an interagency agreement between the U.S. Department of Energy and the Office of the Director of National Intelligence (ODNI). I.C. acknowledges support from the Alfred Spector and Rhonda Kost Fellowship of the Hertz Foundation, the Paul and Daisy Soros Fellowship, and the Department of Defense through the National Defense Science and Engineering Graduate Fellowship Program. YL and E-AK acknowledge New Frontier Grant from Cornell University’s College of Arts and Sciences. The work at MIT (AHK, ITR, WDO) was supported in part by the U.S. Department of Energy, Office of Science, National Quantum Information Science Research Centers, Quantum Systems Accelerator (QSA); and in part by the Defense Advanced Research Projects Agency under the Quantum Benchmarking contract; The computation was done using a high-powered computing cluster established through the support of the Gordon and Betty Moore Foundation’s EPiQS Initiative, Grant GBMF10436 to EAK. The superconducting processor used in the random circuits study was made by the Google Quantum AI team who fabricated the processor, built the cryogenic and control systems, optimized the processor performance, and provided the tools that enabled the execution of this experiment.

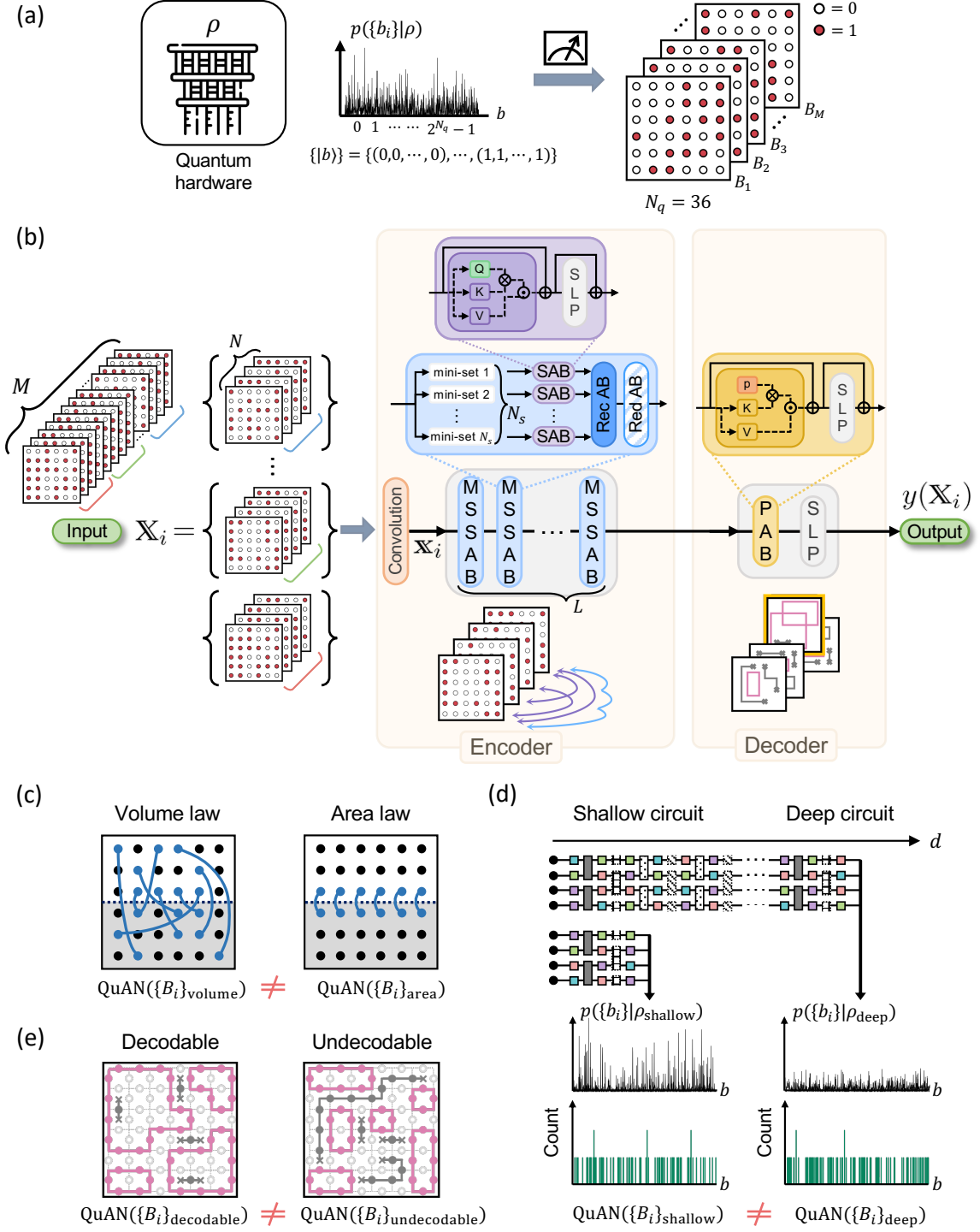


FIG. 1. **Learning relative complexity between states ρ_α and ρ_β from bitstring collections.** (a) Measurements of a quantum state ρ samples bit-strings $\{B_i\}$ from bit-string probability distribution $p(\{b_i\}|\rho)$ over the 2^{N_q} -dimensional Hilbert space. (b) The schematic architecture of QuAN. Z -basis snapshot collection of size M is partitioned into sets $\{X_i\}$ of size N . In the encoder stage, after convolution registers positions of qubits, the set goes through L layers of MSSAB. Inside MSSAB, the input is further partitioned into N_s mini-sets to be parallel processed through SABs, recurrent attention block (RecAB), and reducing attention block (RedAB). The decoder stage compresses output from the encoder, allowing for attending to different components in a permutation-invariant manner, using a PAB and single-layer perception (SLP). The output label is $y = 1$ for state ρ_α and $y = 0$ for state ρ_β . See SM section A for more details. (c-e) Examples of ρ_α and ρ_β for learning relative complexity using binary classification output of QuAN. (c) A volume-law entangled state v.s. an area-law entangled state. The entanglement between two subsystems (white and grey) indicated through blue links. (d) A random circuit state at depth d v.s. that at some deep reference depth. bitstrings shallow and deep circuit states (e) Decodable v.s. undecodable states of an error-correcting code under noise. Incoherent noise depicted in grey suppresses large loops.

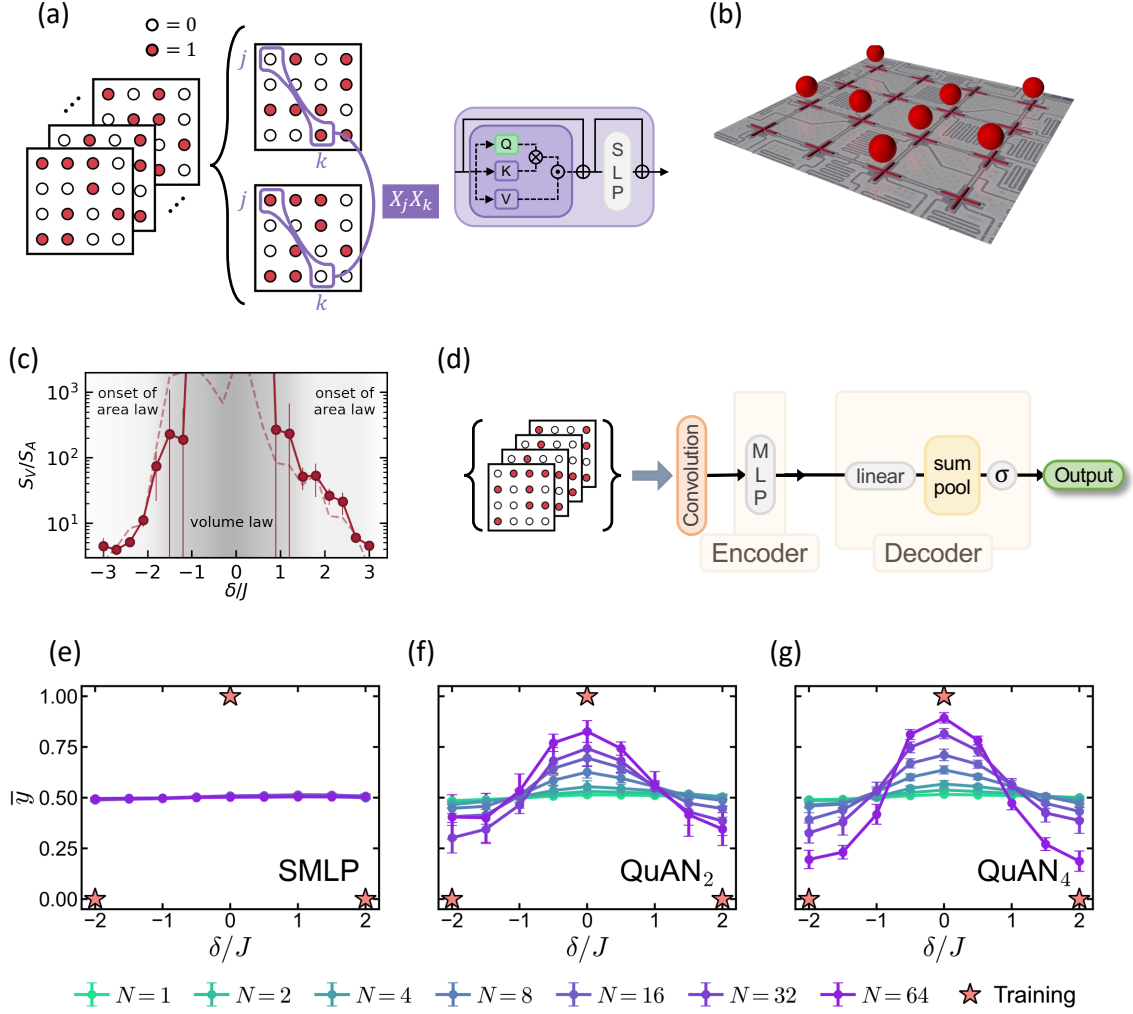


FIG. 2. **Relative complexity between volume-law and area-law scaling states.** (a) Inter-snapshot correlation reveals X - X correlation of the quantum state. The purple box shows the schematic of the self-attention block capturing the inter-snapshot correlation. (b) A schematic diagram of the 16-transmon-qubit chip used for quantum emulation of the driven hard-core Boson-Hubbard model. (c) The entanglement transition based on scaling of bipartite entanglement entropy $S = S_A A + S_V V$, where A and V represent the area and volume of the subsystem, respectively. Adapted from ref. [45]. (d) A schematic of a contrast architecture: the set-multi-layer-perceptron (SMLP) respects the permutation symmetry. (e-g) The average confidence \bar{y} as a function of detuning strength δ for different architectures, using different set size N . The star symbol marks the training points. The average and errors are obtained from 10 independent model training. For machine learning details, see SM section C2. (e) SMLP fails to train. (f) QuAN₂ ($N_s = 1, L = 1$). (g) QuAN₄ with two layers of self-attention ($N_s = 1, L = 2$).

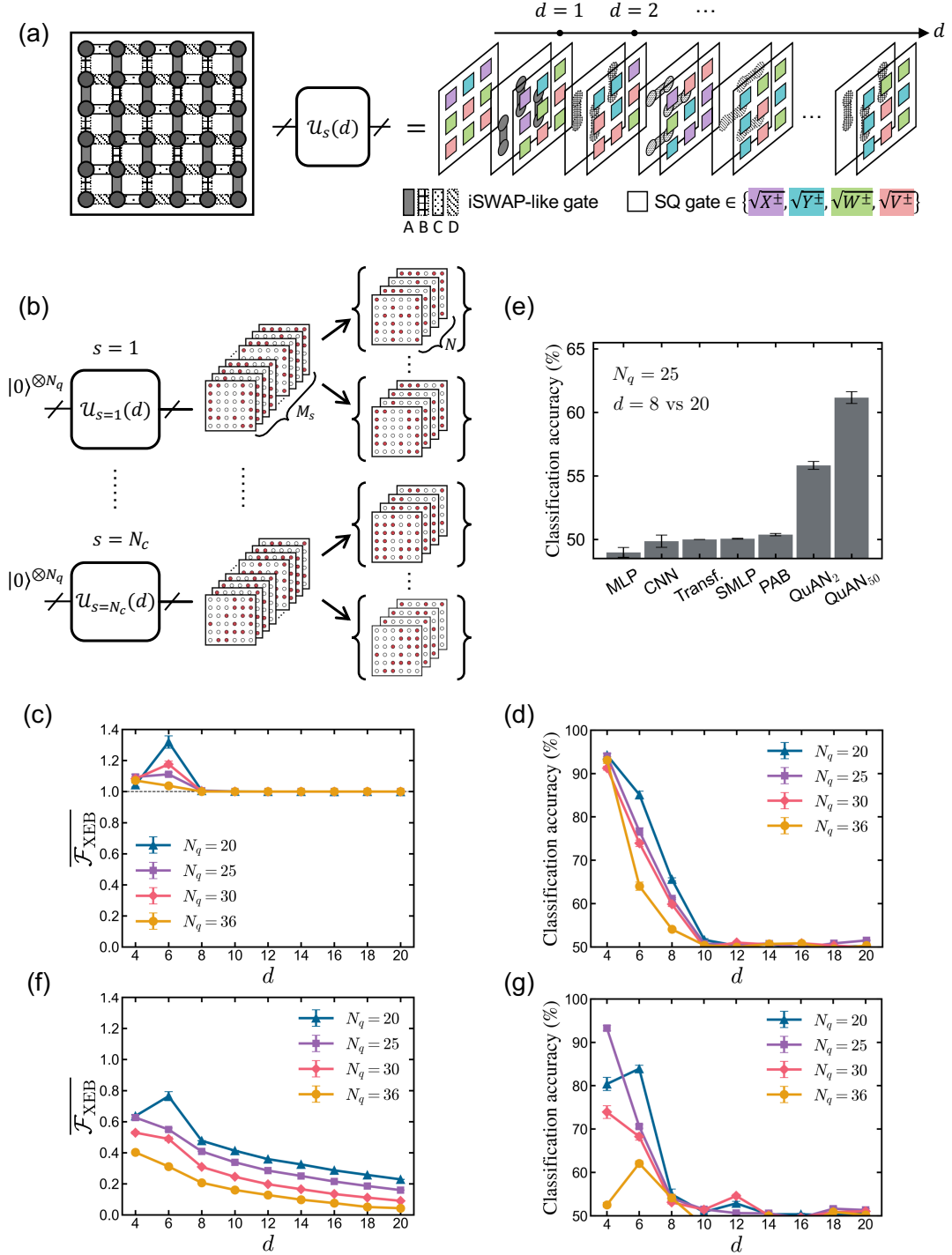


FIG. 3. **Relative complexity between random circuit state at depth d and the reference state at depth $d = 20$.** (a) Schematic illustration of the 6×6 subarray of qubits from Google's "Sycamore" quantum processor. A random circuit of depth d alternates entangling iSWAP-like gates (grey) and single qubit (SQ) gates randomly chosen from the set $\{\sqrt{X}^{\pm 1}, \sqrt{Y}^{\pm 1}, \sqrt{W}^{\pm 1}, \sqrt{V}^{\pm 1}\}$, with $W = (X + Y)/\sqrt{2}$ and $V = (X - Y)/\sqrt{2}$. The two-qubit gates are applied in a repeating series of ABCDCDAB patterns. (b) The data structure. For each depth d , we sample $N_c = 50$ circuits. For each circuit instance s , we sample M_s bit-strings on them into sets of size N , resulting in a total of $N_c \times M_s/N$ sets for each circuit depth d . (c) XEB (Eq. 5) for bit-strings noiseless simulations, as a function of circuit depth d with varying system sizes N_q . The markers show the averaged XEB over $N_c = 50$ different circuit instances and the error bars for the standard errors. (d) The pure-state trained QuAN₅₀'s classification accuracy for pure-state data. We train 8 independent models at each circuit depth d and show the averaged accuracy (marker) and the standard error (error bar). QuAN₅₀ successfully learns the relative complexity of $d = 8$. (e) A comparison of the performances of QuAN₂, QuAN₅₀ and other architectures in learning the relative complexity of depth $d = 8$ on a $N_q = 25$ qubit system. (f) Averaged XEB for experimentally collected bit-strings. The XEB smoothly decays as a function of depth d . (g) Learning relative complexity from experimental data using QuAN₅₀ trained on noiseless data.

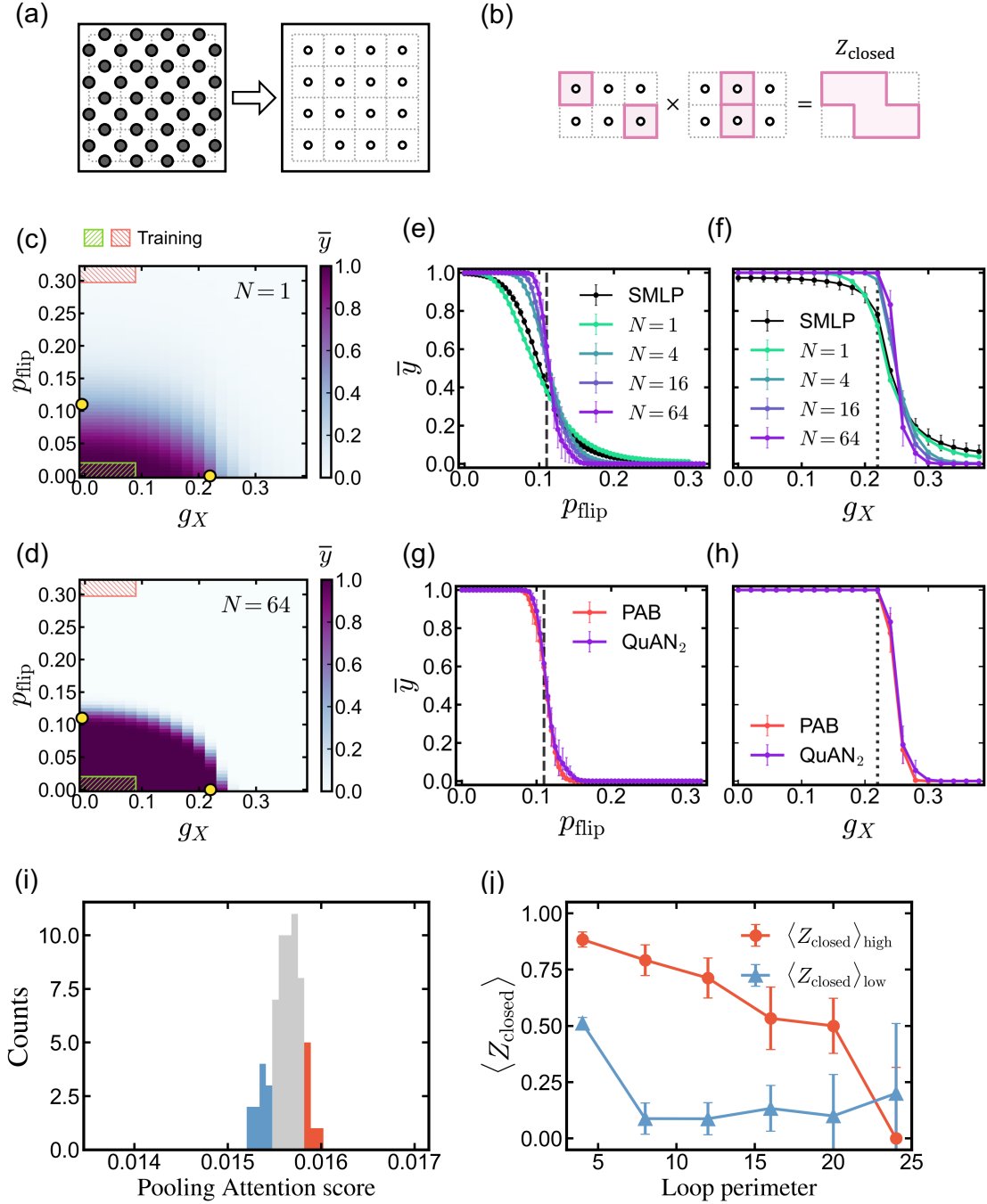


FIG. 4. **Learning the relative complexity of decodable and undecodable states of the toric code.** (a) The transformation from the Z -basis measurements to the smallest-loop, plaquette variables. (b) QuAN can build larger closed loops through multiplication. (c,d) The decodability phase diagram of the toric code state under coherent and incoherent noise for two different set sizes: $N = 1$ in (c) and $N = 64$ in (d). The regions in the phase space that support the training data are marked with hatch marks. The average confidence \bar{y} averages over 10 independent model training. The known thresholds are marked along the $g_X = 0$ axis at $p_c \approx 0.11$ and along the $p_{\text{flip}} = 0$ at $g_c \approx 0.22$. (e) Average confidence \bar{y} by QuAN₂ for different set sizes N , and by SMLP with $N = 64$, along the axis $g_X = 0$. The error bar shows the standard error for \bar{y} over 10 independent model training. (f) Average confidence \bar{y} by QuAN₂ with varying set sizes N , and by SMLP with $N = 64$, along the axis $p_{\text{flip}} = 0$. (g) Average confidence \bar{y} by QuAN₂ and PAB with $N = 64$ along the axis $g_X = 0$, where PAB is defined as the model without self-attention and has only pooling attention. (h) Average confidence \bar{y} by QuAN₂ and PAB with $N = 64$ along the axis $p_{\text{flip}} = 0$. (i) Pooling attention score histogram from the topological state with $(g_X, p_{\text{flip}}) = (0, 0.05)$. (j) The loop expectation value $\langle Z_{\text{closed}} \rangle$ as a function of the loop perimeter, for high and low attention score snapshots in the topological state with $(g_X, p_{\text{flip}}) = (0, 0.05)$. The error bars represent the standard error of $\langle Z_{\text{closed}} \rangle$ over different loop configurations in corresponding snapshots.

- [1] D. Bluvstein, S. J. Evered, A. A. Geim, S. H. Li, H. Zhou, T. Manovitz, S. Ebadi, M. Cain, M. Kalinowski, D. Hangleiter, *et al.*, Logical quantum processor based on reconfigurable atom arrays, *Nature*, 1 (2023).
- [2] Suppressing quantum errors by scaling a surface code logical qubit, *Nature* **614**, 676 (2023).
- [3] Z. Ni, S. Li, X. Deng, Y. Cai, L. Zhang, W. Wang, Z.-B. Yang, H. Yu, F. Yan, S. Liu, *et al.*, Beating the break-even point with a discrete-variable-encoded logical qubit, *Nature* **616**, 56 (2023).
- [4] A. Vaswani, N. Shazeer, N. Parmar, J. Uszkoreit, L. Jones, A. N. Gomez, L. u. Kaiser, and I. Polosukhin, Attention is all you need, in *Advances in Neural Information Processing Systems*, Vol. 30, edited by I. Guyon, U. V. Luxburg, S. Bengio, H. Wallach, R. Fergus, S. Vishwanathan, and R. Garnett (Curran Associates, Inc., 2017).
- [5] A. P. Parikh, O. Täckström, D. Das, and J. Uszkoreit, A Decomposable Attention Model for Natural Language Inference (2016), arXiv:1606.01933 [cs].
- [6] L. Susskind, Computational complexity and black hole horizons, *Fortschritte der Physik* **64**, 24 (2016).
- [7] A. R. Brown and L. Susskind, Second law of quantum complexity, *Physical Review D* **97**, 086015 (2018).
- [8] A. Bouland, B. Fefferman, and U. Vazirani, Computational pseudorandomness, the wormhole growth paradox, and constraints on the AdS/CFT duality (2019), arxiv:1910.14646 [gr-qc, physics:hep-th, physics:quant-ph].
- [9] S. Aaronson, Y. Atia, and L. Susskind, On the Hardness of Detecting Macroscopic Superpositions (2020), arxiv:2009.07450 [gr-qc, physics:quant-ph].
- [10] D. Gross, S. T. Flammia, and J. Eisert, Most Quantum States Are Too Entangled To Be Useful As Computational Resources, *Physical Review Letters* **102**, 190501 (2009).
- [11] D. Girolami and F. Anzà, Quantifying the Difference between Many-Body Quantum States, *Physical Review Letters* **126**, 10.1103/physrevlett.126.170502 (2021).
- [12] M. B. Hastings, Topological Order at Nonzero Temperature, *Physical Review Letters* **107**, 210501 (2011).
- [13] M. Schwarz, K. Temme, F. Verstraete, D. Perez-Garcia, and T. S. Cubitt, Preparing topological projected entangled pair states on a quantum computer, *Physical Review A* **88**, 10.1103/physreva.88.032321 (2013).
- [14] J. Miller and A. Miyake, Latent Computational Complexity of Symmetry-Protected Topological Order with Fractional Symmetry, *Physical Review Letters* **120**, 10.1103/physrevlett.120.170503 (2018).
- [15] F. G. Brandão, W. Chemissany, N. Hunter-Jones, R. Kueng, and J. Preskill, Models of Quantum Complexity Growth, *PRX Quantum* **2**, 030316 (2021), publisher: American Physical Society.
- [16] J. Haferkamp, P. Faist, N. B. T. Kothakonda, J. Eisert, and N. Yunger Halpern, Linear growth of quantum circuit complexity, *Nature Physics* **18**, 528 (2022).
- [17] K. Kaneko, E. Iyoda, and T. Sagawa, Characterizing complexity of many-body quantum dynamics by higher-order eigenstate thermalization, *Physical Review A* **101**, 10.1103/physreva.101.042126 (2020).
- [18] E. Bianchi, L. Hackl, M. Kieburg, M. Rigol, and L. Vidmar, Volume-Law Entanglement Entropy of Typical Pure Quantum States, *PRX Quantum* **3**, 10.1103/prxquantum.3.030201 (2022).
- [19] J. Wang, M. H. Lamann, J. Richter, R. Steinigeweg, A. Dymarsky, and J. Gemmer, Eigenstate Thermalization Hypothesis and Its Deviations from Random-Matrix Theory beyond the Thermalization Time, *Physical Review Letters* **128**, 10.1103/physrevlett.128.180601 (2022).
- [20] B. D. S. L. Torres and E. Martín-Martínez, Toward a physically motivated notion of Gaussian complexity geometry, *Physical Review D* **110**, 10.1103/physrevd.110.025006 (2024).
- [21] H. A. Camargo, L. Hackl, M. P. Heller, A. Jahn, T. Takayanagi, and B. Windt, Entanglement and complexity of purification in (1+1)-dimensional free conformal field theories, *Physical Review Research* **3**, 10.1103/physrevresearch.3.013248 (2021).
- [22] N. Yunger Halpern, N. B. T. Kothakonda, J. Haferkamp, A. Munson, J. Eisert, and P. Faist, Resource theory of quantum uncomplexity, *Physical Review A* **106**, 062417 (2022).
- [23] C. Miles, R. Samajdar, S. Ebadi, T. T. Wang, H. Pichler, S. Sachdev, M. D. Lukin, M. Greiner, K. Q. Weinberger, and E.-A. Kim, Machine learning discovery of new phases in programmable quantum simulator snapshots, *Physical Review Research* **5**, 013026 (2023), publisher: American Physical Society.
- [24] H.-Y. Huang, R. Kueng, G. Torlai, V. V. Albert, and J. Preskill, Provably efficient machine learning for quantum many-body problems, *Science* **377**, eabk3333 (2022).
- [25] C. Miles, A. Bohrdt, R. Wu, C. Chiu, M. Xu, G. Ji, M. Greiner, K. Q. Weinberger, E. Demler, and E.-A. Kim, Correlator convolutional neural networks as an interpretable architecture for image-like quantum matter data, *Nature Communications* **12**, 3905 (2021).
- [26] J. Carrasquilla, Machine learning for quantum matter, *Advances in Physics: X* **5**, 1797528 (2020), publisher: Taylor & Francis eprint: <https://doi.org/10.1080/23746149.2020.1797528>.
- [27] Y. Zhang, P. Ginsparg, and E.-A. Kim, Interpreting machine learning of topological quantum phase transitions, *Physical Review Research* **2**, 023283 (2020).
- [28] Y. Zhang, R. G. Melko, and E.-A. Kim, Machine learning Z₂ quantum spin liquids with quasiparticle statistics, *Physical Review B* **96**, 245119 (2017).
- [29] Y. Zhang and E.-A. Kim, Quantum Loop Topography for Machine Learning, *Physical Review Letters* **118**, 216401 (2017).
- [30] S. Ahmed, C. Sánchez Muñoz, F. Nori, and A. F. Kockum, Quantum State Tomography with Conditional Generative Adversarial Networks, *Physical Review Letters* **127**, 140502 (2021), publisher: American Physical Society.
- [31] M. Y. Niu, A. M. Dai, L. Li, A. Odena, Z. Zhao, V. Smelyanskiy, H. Neven, and S. Boixo, Learnability and complexity of quantum samples (2020), arXiv:2010.11983 [quant-ph].
- [32] P. Cha, P. Ginsparg, F. Wu, J. Carrasquilla, P. L. McMahon, and E.-A. Kim, Attention-based quantum tomography, *Machine Learning: Science and Technology* **3**,

- 01LT01 (2021), publisher: IOP Publishing.
- [33] J. Carrasquilla, G. Torlai, R. G. Melko, and L. Aolita, Reconstructing quantum states with generative models, *Nature Machine Intelligence* **1**, 155 (2019), number: 3 Publisher: Nature Publishing Group.
- [34] J. Carrasquilla, D. Luo, F. Pérez, A. Miled, B. K. Clark, M. Volkovs, and L. Aolita, Probabilistic simulation of quantum circuits using a deep-learning architecture, *Physical Review A* **104**, 032610 (2021).
- [35] Y.-H. Zhang and M. Di Ventura, Transformer quantum state: A multipurpose model for quantum many-body problems, *Physical Review B* **107**, 075147 (2023), publisher: American Physical Society.
- [36] F. G. S. L. Brandão, A. W. Harrow, and M. Horodecki, Local Random Quantum Circuits are Approximate Polynomial-Designs, *Communications in Mathematical Physics* **346**, 397 (2016).
- [37] J. Haferkamp, Random quantum circuits are approximate unitary t -designs in depth $O(\log(n^{5+o(1)}))$, *Quantum* **6**, 795 (2022).
- [38] J. Lee, Y. Lee, J. Kim, A. Kosiorek, S. Choi, and Y. W. Teh, Set Transformer: A Framework for Attention-based Permutation-Invariant Neural Networks, in *Proceedings of the 36th International Conference on Machine Learning* (PMLR, 2019) pp. 3744–3753, iSSN: 2640-3498.
- [39] D. N. Page, Average entropy of a subsystem, *Physical Review Letters* **71**, 1291 (1993).
- [40] Y. Li, X. Chen, and M. P. A. Fisher, Measurement-driven entanglement transition in hybrid quantum circuits, *Physical Review B* **100**, 134306 (2019).
- [41] B. Skinner, J. Ruhman, and A. Nahum, Measurement-Induced Phase Transitions in the Dynamics of Entanglement, *Physical Review X* **9**, 031009 (2019), publisher: American Physical Society.
- [42] C.-M. Jian, Y.-Z. You, R. Vasseur, and A. W. W. Ludwig, Measurement-induced criticality in random quantum circuits, *Physical Review B* **101**, 104302 (2020), publisher: American Physical Society.
- [43] M. J. Gullans and D. A. Huse, Dynamical Purification Phase Transition Induced by Quantum Measurements, *Physical Review X* **10**, 041020 (2020), publisher: American Physical Society.
- [44] S. Choi, Y. Bao, X.-L. Qi, and E. Altman, Quantum Error Correction in Scrambling Dynamics and Measurement-Induced Phase Transition, *Physical Review Letters* **125**, 030505 (2020).
- [45] A. H. Karamlou, I. T. Rosen, S. E. Muschinske, C. N. Barrett, A. Di Paolo, L. Ding, P. M. Harrington, M. Hays, R. Das, D. K. Kim, B. M. Niedzielski, M. Schuld, K. Serniak, M. E. Schwartz, J. L. Yoder, S. Gustavsson, Y. Yanay, J. A. Grover, and W. D. Oliver, Probing entanglement in a 2D hard-core Bose–Hubbard lattice, *Nature* 10.1038/s41586-024-07325-z (2024).
- [46] M. M. Wolf, F. Verstraete, M. B. Hastings, and J. I. Cirac, Area laws in quantum systems: Mutual information and correlations, *Phys. Rev. Lett.* **100**, 070502 (2008).
- [47] I. Goodfellow, Y. Bengio, and A. Courville, *Deep learning* (MIT press, 2016).
- [48] P. Hayden and J. Preskill, Black holes as mirrors: Quantum information in random subsystems, *Journal of High Energy Physics* **2007**, 120 (2007).
- [49] A. Nahum, J. Ruhman, S. Vijay, and J. Haah, Quantum Entanglement Growth under Random Unitary Dynamics, *Physical Review X* **7**, 031016 (2017).
- [50] C. W. Von Keyserlingk, T. Rakovszky, F. Pollmann, and S. L. Sondhi, Operator Hydrodynamics, OTOCs, and Entanglement Growth in Systems without Conservation Laws, *Physical Review X* **8**, 021013 (2018).
- [51] A. Nahum, S. Vijay, and J. Haah, Operator Spreading in Random Unitary Circuits, *Physical Review X* **8**, 021014 (2018).
- [52] By correct classification in mean the machine’s confidence in the correct labels exceeding 0.5.
- [53] E. Dennis, A. Kitaev, A. Landahl, and J. Preskill, Topological quantum memory, *Journal of Mathematical Physics* **43**, 4452 (2002), arXiv:quant-ph/0110143.
- [54] Y. Bao, R. Fan, A. Vishwanath, and E. Altman, Mixed-state topological order and the errorfield double formulation of decoherence-induced transitions (2023), arXiv:2301.05687 [cond-mat, physics:quant-ph].
- [55] R. Fan, Y. Bao, E. Altman, and A. Vishwanath, Diagnostics of mixed-state topological order and breakdown of quantum memory (2023), arXiv:2301.05689 [cond-mat, physics:quant-ph].
- [56] Y.-H. Chen and T. Grover, Unconventional topological mixed-state transition and critical phase induced by self-dual coherent errors, arXiv preprint arXiv:2403.06553 (2024).
- [57] R. Sohal and A. Prem, A noisy approach to intrinsically mixed-state topological order, arXiv preprint arXiv:2403.13879 (2024).
- [58] M. B. Hastings and X.-G. Wen, Quasiadiabatic continuation of quantum states: The stability of topological ground-state degeneracy and emergent gauge invariance, *Physical review b* **72**, 045141 (2005).
- [59] C. Castelnovo and C. Chamon, Topological order and topological entropy in classical systems, *Physical Review B* **76**, 174416 (2007).
- [60] A. Honecker, M. Picco, and P. Pujol, Universality class of the nishimori point in the $2d \pm j$ random-bond ising model, *Physical review letters* **87**, 047201 (2001).
- [61] N. Maskara, Enhancing detection of topological order by local error correction.
- [62] I. Cong, N. Maskara, M. C. Tran, H. Pichler, G. Semeghini, S. F. Yelin, S. Choi, and M. D. Lukin, Enhancing detection of topological order by local error correction, *Nature Communications* **15**, 1527 (2024).
- [63] C. Castelnovo and C. Chamon, Quantum topological phase transition at the microscopic level, *Physical Review B* **77**, 054433 (2008).
- [64] This expectation value can be readily calculated from each subset of Z -basis snapshots as an average.

Supplementary Materials for “Attention to Quantum Complexity”

Hyejin Kim^{†,1} Yiqing Zhou^{†,1} Yichen Xu^{†,1} Kaarthik Varma,¹ Amir H. Karamlou,²
Ilan T. Rosen,³ Jesse C. Hoke,^{4,5} Chao Wan,⁶ Jin Peng Zhou,⁶ William D.
Oliver,^{2,3,7} Yuri D. Lensky,^{1,4} Kilian Q. Weinberger,⁶ and Eun-Ah Kim^{1,4,8,*}

¹*Department of Physics, Cornell University, Ithaca, NY, USA*

²*Department of Physics, Massachusetts Institute of Technology, Cambridge, MA 02139, USA*

³*Research Laboratory of Electronics, Massachusetts Institute of Technology, Cambridge, MA 02139, USA*

⁴*Google Research, Mountain View, CA, USA*

⁵*Department of Physics, Stanford University, Stanford, CA, USA*

⁶*Department of Computer Science, Cornell University, Ithaca, New York 14853, USA*

⁷*Department of Electrical Engineering and Computer Science,
Massachusetts Institute of Technology, Cambridge, MA 02139, USA*

⁸*Department of Physics, Ewha Womans University, Seoul, South Korea*

[†]*These authors contributed equally to this work.*

(Dated: November 22, 2024)

CONTENTS

A. QuAN Architecture	2
1. Input	2
2. Convolution	2
3. Mini-set Self-attention block (MSSAB) Encoder	3
a. Parallel SAB	3
b. Recurrent AB (RecAB)	5
c. Reducing AB (RedAB)	5
d. Computational complexity of MSSAB	5
4. Pooling Attention Block (PAB) Decoder	7
B. Comparison of QuAN and other ML architectures	8
C. Driven Hard-core Bose-Hubbard model	10
1. Data acquisition	10
2. Data preprocessing	10
3. Training and testing procedure	11
4. Machine learning details	12
5. Correlation as a witness of entanglement	13
D. Random quantum circuit	14
1. Data acquisition	14
a. Quantum processor details and experimental procedure	14
b. Simulation and linear cross-entropy benchmarking (XEB)	14
2. Data preprocessing	15
3. Training and testing procedure	15
4. Machine learning details	16
5. Circuit depth and moments of the bitstring distribution	19
E. Toric code simulation	20
1. Data acquisition	20
2. Data preprocessing	20
3. Training and testing procedure	20
4. Benchmarking machine results	21

* Corresponding author: eun-ah.kim@cornell.edu

a. Benchmarking to locally error-corrected decoration (LED)	21
b. Benchmarking to SMLP	23
5. Machine analysis: PAB as an importance-sampler	24
References	26

Appendix A: QuAN Architecture

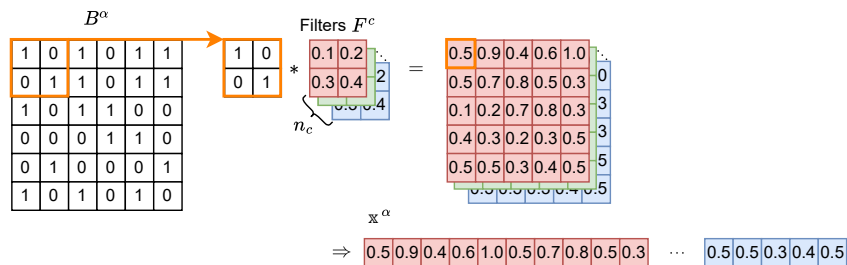
Capturing quantum fluctuation and respecting samples' permutation invariance is essential to learn information about quantum states from measurement snapshots. Here, we introduce QuAN, a machine learning model which uses attention mechanism [1] to learn inter-snapshot correlations while respecting the permutation invariance of the snapshots [2, 3]. Learning high-order moments can be a practical way of learning characteristics of the distribution of bit-strings. However, direct application of existing self-attention blocks, as in Ref. [3], is inefficient and allows us to access only low-order moments. To study complex quantum systems where high-order moments become crucial, we propose (in Section A 3) a new encoding scheme, named mini-set self-attention block (MSSAB), that can efficiently sample high-order correlations with low computational cost.

In this section, we present details of the inner structure of QuAN. A detailed structure of QuAN architecture is presented in the main text Fig. 1(e). The rest of this section is organized as follows: First, in Section A 1, we discuss the input data structure taken by QuAN. Second, we discuss in Section A 2 the usage of a two-dimensional convolution layer and any preprocessing of the raw measurement snapshots before inputting into the encoder. Third, we discuss in Section A 3 how the workhorse in QuAN - the mini-set self-attention block (MSSAB) is used in the encoder to capture inter-snapshot correlations. Lastly, we discuss in Section A 4 the pooling attention block (PAB) in the decoder.

1. Input

QuAN takes a *set* of two-dimensional bit-string of N_q qubits as input data, where each bit-string consists of N_q binary values (0 or 1). We denote the inputs to QuAN, which are i -th set (datapoint) $\mathbf{X}_i = \{B_{i,\alpha}\}_{\alpha=1}^N$ consisting of N two-dimensional binary-valued arrays $B_{i,\alpha}$, where α indexes the elements within the set and N is the set size. (Each binary-valued array has N_q entries indexed by μ , i.e. $B_{i,\alpha,\mu} = 0$ or 1. To avoid confusion between the set element index $\alpha \in \{1, \dots, N\}$ and the spatial dimension index $\mu \in \{1, \dots, N_q\}$, we relocate the index α from superscript to subscript, s.t. $B_{i,\mu}^\alpha \equiv B_{i,\alpha,\mu}$.) Once \mathbf{X}_i is inputted into QuAN, the output is given by $y(\mathbf{X}_i)$, and QuAN is optimized through binary cross entropy loss $\mathcal{L} = -\sum_i \hat{y}_i \log y(\mathbf{X}_i)$ between true label \hat{y}_i and output.

2. Convolution



SFig. 1: Schematic example of convolution layer applied to $N_q = 36$ bit-string with $N_r = 6$ rows and $N_c = 6$ columns. Convolution operation denoted as ‘*’ involves summing over element-wise multiplication of part of bit-string and convolution filter. n_c represents the number of 2×2 convolution filter, and \mathbf{x}^α is the output after flattening convolution output into vector. We use a stride of 1 and no padding.

The original input data are sets of binary-valued arrays. We first pass the input sets through a convolution layer (see SFig. 1). The convolution step has two purposes: First, the original binary-valued arrays are mapped to vectors with continuous entries with better algebraic properties, illustrated in SFig. 1. Second, the convolution enables the

model to capture possible local spatial features. In the convolution layer, we apply convolution filter $\{F^c\}_{c=1}^{n_c}$ of kernel size `kernel` = 2 and stride 1, on each two-dimensional bit-string array of N_r rows and N_c columns. The channel number n_c is a hyperparameter of the ML model that controls the numbers of 2×2 filters. After the convolution layer, `BatchNorm2d` over set elements follows. The resulting output is then flattened into a 1D vector. The dimension of 1D vector d_x depends on the convolution layer hyperparameters; $d_x = n_c(N_r - \text{kernel} + 1)(N_c - \text{kernel} + 1)$. We use a stride of 1 and no padding in this paper. The output of the convolution layer $\mathbf{x}_\mu^\alpha \equiv \mathbf{x}_{i,\mu}^\alpha$ is a matrix of size (N, d_x) , where $\alpha = 1, \dots, N$ and $\mu = 1, \dots, d_x$.

3. Mini-set Self-attention block (MSSAB) Encoder

The encoder aims to transform its input into a more informative representation, which will be further used in the following decoder block to accomplish the desired task — in our case, the binary classification task. When designing the encoder architecture, we consider two key insights into the data of interest: First, we expect the high-order moments of the bit-string distribution to contain important information. Second, we expect the ordering of the snapshots to be irrelevant since each measurement is drawn independently.

The first insight, the desire to capture high-order moments, motivates us to utilize the attention mechanism. The attention mechanism first introduced in Ref. [1] drives the success of transformers as the core of large language models. The attention mechanism lets the models learn correlations between words (or tokens) in sentences. However, direct usage of the vanilla attention mechanism brings us limited power since the model will view the input bit-strings as a sequence and will try to learn from their ordering.

To overcome this limitation, we must consider the second insight, the permutation invariance of the input bit-strings. Building on the vanilla attention mechanism [1], Ref. [3] introduces a permutation invariant version of transformer, named set transformer, since it treats the input as a set, instead of a sequence. We follow the convention of the set transformer [3] and call the self-attention module respecting permutation invariance the self-attention block (SAB). Although, in theory, SAB can capture correlations while respecting permutation invariance, a long sequence of stacked SABs is needed for the model to access high-order moments, which soon becomes impractical.

We introduce MSSAB as a parameter-efficient and practical version of SAB when accessing high-order inter-snapshot correlation between bit-strings. While the SAB [3] considers *all-to-all* second-order inter-snapshot correlations between input set elements, our MSSAB *samples* higher-order inter-snapshot correlations and thus greatly reduces the computational cost. A single-layer of MSSAB is structured into three key components: a parallel self-attention block (SAB), a recurrent attention block (RecAB), and a reducing attention block (RedAB) (see main text Fig. 1(e) encoder and SFig. 2). Each of these components plays a crucial role in the functionality of MSSAB. We discuss each part in more detail in Sections A 3 a, A 3 b, A 3 c. Finally, we compare the computational complexity of MSSAB with SAB in Section A 3 d.

a. Parallel SAB

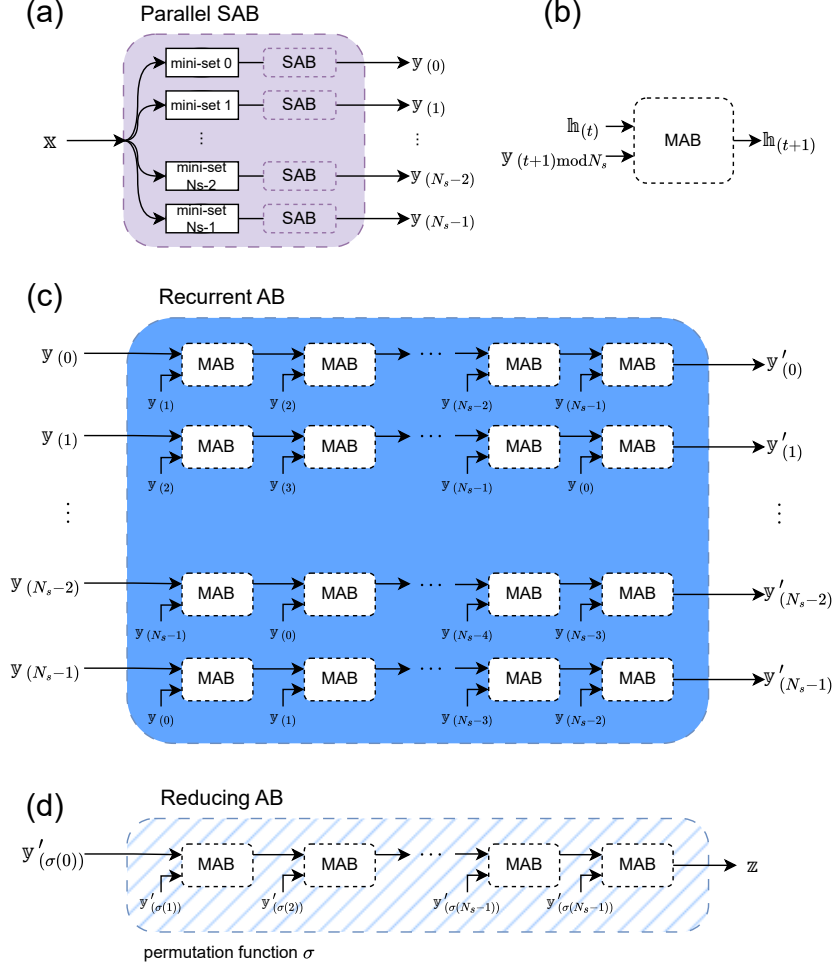
First, the input set is shuffled and partitioned into N_s mini-sets, where N_s is the number of mini-sets and is the core hyperparameter of MSSAB. The parallel SAB transforms each mini-set independently. Note that the input set to the encoder is the output of the previous convolution layer.

The parallel SAB block is shown as the purple block in main text Fig. 1(e), and the inner structure in SFig. 2(a). We first perform a preprocessing strategy called ‘mini-set partitioning,’ which is a partition of the input set (set size N) into N_s subsets of size N/N_s , called mini-sets. These mini-sets allow for parallel processing. The main objective of parallel SAB is to capture pairwise second-order correlation only within each mini-set.

The essential unit in parallel SAB is the self-attention block (SAB) that allows access to second-order moments between bit-strings, which we will discuss at the end of this paragraph. In the main text, we introduce the simplified version of the self-attention score for a set of snapshots \mathbf{X}_i (see main text Eq. (1)). For actual implementation, we use the output of convolution layer $\mathbf{x}_i = F^c(\mathbf{X}_i)$ instead of bare snapshots,

$$\langle Q_{\mathbf{x}_i} | K_{\mathbf{x}_i} \rangle = (Q_{\mathbf{x}_i})(K_{\mathbf{x}_i})^T \quad (\text{A1})$$

up to normalization. We will omit index i for convenience. The input to the encoder is denoted as \mathbf{x}_μ^α where α indexes the set element and μ represents the dimension of the feature space after the previous convolution layer. We will use the Greek letter α, β to represent a set index running from 1 to N and $\mu, \nu, \rho, \lambda, \eta$ for the feature space index running



SFig. 2: Details of various blocks in the QuAN architecture. (a) The inner structure of parallel self-attention block (SAB). (b) Multihead-attention block (MAB) inside recurrent and reducing attention block (RecAB, RedAB). (c) The inner structure of recurrent attention block (RecAB). (d) The inner structure of reducing attention block (RedAB). $\sigma : S \rightarrow S$ is the random permutation function that permutes mini-set index $S = \{0, 1, \dots, N_s - 1\}$.

from 1 to d_h (or d_x). SAB transforms the input set to a set of hidden state vectors:

$$\mathbf{h}_\mu^\alpha = \sum_{\nu} Q_{\mu\nu} \mathbf{x}_\nu^\alpha + \sum_{\beta=1}^N \text{Softmax} \left[\sum_{\rho} \sum_{\lambda\eta} \frac{1}{\sqrt{d_h}} (Q_{\rho\lambda} \mathbf{x}_\lambda^\alpha K_{\rho\eta} \mathbf{x}_\eta^\beta) \right] \sum_{\nu} V_{\mu\nu} \mathbf{x}_\nu^\beta, \quad (\text{A2})$$

with the hidden dimension size d_h . Q , K and V are query, key, and value matrices of dimensions (d_h, d_x) . To gain insight into how the model learns important relevant features, we rewrite the above expression in the following form:

$$A^{\alpha\beta} = \text{Softmax} \left[\sum_{\rho\lambda\eta} \frac{1}{\sqrt{d_h}} (Q_{\rho\lambda} \mathbf{x}_\lambda^\alpha K_{\rho\eta} \mathbf{x}_\eta^\beta) \right] \sim \text{Softmax} [\mathbf{x}^\alpha \cdot \mathbf{x}^\beta], \quad (\text{A3})$$

$$\mathbf{h}_\mu^\alpha = \sum_{\beta} A^{\alpha\beta} \left(\sum_{\nu} Q_{\mu\nu} \mathbf{x}_\nu^\alpha + V_{\mu\nu} \mathbf{x}_j^\beta \right), \quad (\text{A4})$$

where $\sum_{\beta} A^{\alpha\beta} = 1$. The self-attention score matrix $A^{\alpha\beta}$ is of dimensions (N, N) . Calculating the self-attention score involves two set elements (\mathbf{x}^α and \mathbf{x}^β), which can capture all-to-all second-order moments in \mathbf{x} . This is followed by

layer normalization on spatial dimension and a linear layer:

$$\begin{aligned} \mathbf{h}'_{\mu} &= \text{LayerNorm}(\mathbf{h}_{\mu}^{\alpha}), \\ \mathbf{y}'_{\mu} &= \text{Sigmoid}(\text{LayerNorm}(\mathbf{h}'_{\mu} + \text{FF}_{\mu\nu}(\mathbf{h}'_{\nu}))), \end{aligned} \quad (\text{A5})$$

where FF is a feed-forward function for residual connection that acts on each set element equally, which in our implementation is to multiply by a matrix O of dimensions (d_h, d_h) followed by activation function (either Sigmoid or ReLU), i.e. $\text{FF}(\mathbf{x}) = \text{ReLU}(O\mathbf{x})$ or $\text{Sigmoid}(O\mathbf{x})$ for each set element \mathbf{x} . Q, K, V, O are learned weight matrices in SAB. The output of SAB, \mathbf{y}'_i^{α} , is a matrix of dimensions (N, d_h) .

There are N_s parallel SABs acting on N_s mini-set, where parameters are shared across all the SAB blocks. We denote the output of parallel SAB as $\{\mathbf{y}_{(0)}, \dots, \mathbf{y}_{(N_s-1)}\}$, where the subscript with parentheses is the mini-set label. Each output $\mathbf{y}_{(m)}$ is a matrix of size $(N/N_s, d_h)$. Parallel SAB can access second-order moments of a bit-string distribution within each mini-set, unlike ordinary SAB accessing all-to-all second-order moments.

b. Recurrent AB (RecAB)

The RecAB takes the outputs of parallel SAB, and attends them recurrently with multiple randomized orderings. A schematic of RecAB is shown as the blue block in Fig. 1(e), and the inner structure is plotted in SFig. 2(c). RecAB was devised to capture correlations between different mini-sets that were not captured through parallel SAB; by attending mini-sets $\{\mathbf{y}_{(0)}, \dots, \mathbf{y}_{(N_s-1)}\}$ recurrently, RecAB can capture up to $2N_s$ -th order correlation in \mathbf{x} .

We utilize multihead-attention block (MAB) instead of SAB since we compute the attention score between two different mini-sets. Each (parallel SAB output) mini-set $\mathbf{y}_{(m)}$ goes into $N_s - 1$ MABs. At each time t attended by the next mini-set $\mathbf{y}_{((m+t+1)\bmod N_s)}$, where MAB is given by

$$\mathbf{h}_{(t+1),\mu}^{\alpha} = \sum_{\nu} Q'_{\mu\nu} \mathbf{y}_{((m+t+1)\bmod N_s),\nu}^{\alpha} + \sum_{\beta=1}^{N/N_s} \text{Softmax} \left[\sum_{\rho\lambda\eta} \frac{1}{\sqrt{d_h}} \left(Q'_{\rho\lambda} \mathbf{y}_{((m+t+1)\bmod N_s),\lambda}^{\alpha} K'_{\rho\eta} \mathbf{h}_{(t),\eta}^{\beta} \right) \right] \sum_{\nu} V'_{\mu\nu} \mathbf{h}_{(t),\nu}^{\beta}, \quad (\text{A6})$$

where $\mathbf{h}_{(0)} \equiv \mathbf{y}_{(m)}$, $\mathbf{h}_{(N_s-1)} \equiv \mathbf{y}'_{(m)}$. Attention score between two different mini-sets involves two set elements $\mathbf{y}_{(m)}^{\alpha}$ and $\mathbf{y}_{(m')}^{\beta}$ each from m and m' -th mini-set, hence capturing the second-order correlation between two mini-sets. Each MAB operation is independent and identical, followed by the same layers as in Eq. (A5). We denote the output of RecAB as $\{\mathbf{y}'_{(0)}, \dots, \mathbf{y}'_{(N_s-1)}\}$. Each output $\mathbf{y}'_{(m)}$ is a matrix of size $(N/N_s, d_h)$. While each mini-set passes through $N_s - 1$ numbers of MAB recurrently, it involves N_s set elements each from different mini-set ($\mathbf{y}_{(m)}^{\alpha_0}, \mathbf{y}_{(m+1)}^{\alpha_1}, \dots, \mathbf{y}_{((m+N_s-1)\bmod N_s)}^{\alpha_{N_s-1}}$), which can capture N_s -th order moment in \mathbf{y} . In other words, RecAB can access $2N_s$ -th order moments in \mathbf{x} , considering \mathbf{y} contains second-order moment information of \mathbf{x} .

c. Reducing AB (RedAB)

Finally, the RedAB attends mini-sets in a randomized sequence and shrinks N_s mini-sets into one.

The RedAB is shown as the blue dashed block in Fig. 1(e), and the inner structure is plotted in SFig. 2(d). RedAB is designed to reduce all (RecAB output) mini-sets into a single mini-set while preserving the mini-set permutation invariance. We attend mini-sets $\{\mathbf{y}'_{(0)}, \dots, \mathbf{y}'_{(N_s-1)}\}$ in a randomized sequence using $N_s - 1$ MABs (each MAB operation is independent and identical, followed by the same layers as in Eq. (A5); we use the same MAB from RecAB.) Similar to RecAB, RedAB with $N_s - 1$ numbers of MAB involves N_s set elements from different mini-set ($\mathbf{y}'_{(\sigma(0))}^{\beta_0}, \mathbf{y}'_{(\sigma(1))}^{\beta_1}, \dots, \mathbf{y}'_{(\sigma(N_s-1))}^{\beta_{N_s-1}}$ where σ is a randomized permutation function), which captures N_s -th order moment in \mathbf{y}' . In other words, RedAB can access $2N_s^2$ -th order moments in \mathbf{x} . The final output of RedAB is $\mathbf{z} \equiv \mathbf{z}_{\mu}^{\alpha}$, a matrix of dimensions $(N/N_s, d_h)$ with $\alpha = 1, \dots, N/N_s$ and $\mu = 1, \dots, d_h$. Therefore, one MSSAB layer reduces the input set size N to N/N_s .

d. Computational complexity of MSSAB

MSSAB is more parameter-efficient when we need to target high-order moments. In this subsection, we discuss the computational complexity of MSSAB and compare it to the SAB [3]. Note that MSSAB with no mini-set partitioning ($N_s = 1$) reduces to ordinary SAB.

First, we walk through how the MSSAB collects increasing order of moments through the parallel-SAB, RecSAB, and RedSAB sequence and finally reaches up to $(2N_s^2)$ -th moments in its output.

Parallel-SAB - In parallel-SAB block, each mini-set passes through one layer of SAB (see SFig. 2(a)). The transformation performed in SAB is shown in Eq. (A2), where two set elements are involved in the calculation of attention score (see Eq. (A3)), so the outputs $\{\mathbf{y}_{(m)}\}_{m=0}^{N_s-1}$ samples up to 2-nd order moments of the input set \mathbf{x} . For simplicity, we define $\text{Order}(\cdot)$ to be the order of moments (\cdot) can access. Thus, $\text{Order}(\mathbf{y}_{(m)}) = 2$ for $\mathbf{y}_{(m)} \in \{\mathbf{y}_{(m)}\}_{m=0}^{N_s-1}$.

RecAB - The RecAB attends each of $\{\mathbf{y}_{(m)}\}_{m=0}^{N_s-1}$ with others, resulting in $\{\mathbf{y}'_{(m)}\}_{m=0}^{N_s-1}$. Calculating the order of moments is more convenient if we consider the recurrent representation, as shown in SFig. 2(b). Recursively, we have

$$\text{Order}(\mathbf{h}_{(t+1)}) = \text{Order}(\mathbf{h}_{(t)}) + \text{Order}(\mathbf{y}_{(t+1) \bmod N_s}) \quad (\text{A7})$$

$$= \text{Order}(\mathbf{h}_{(t)}) + 2, \quad (\text{A8})$$

$$\text{Order}(\mathbf{h}_{(0)}) = \text{Order}(\mathbf{y}_{(m)}) = 2. \quad (\text{A9})$$

Via recursion unrolling, we have $\text{Order}(\mathbf{h}_{N_s-1}) = 2N_s$. As shown in the unrolled flowchart of RecAB (SFig. 2(c)), each row represents a different ordering of $\{\mathbf{y}_{(m)}\}_{m=0}^{N_s-1}$ in which the attention mechanism attends. That is, we initialize $\mathbf{h}_{(0)}$ with N_s different mini-sets, each gives an output among $\{\mathbf{y}'_{(m)}\}_{m=0}^{N_s-1}$. Thus,

$$\text{Order}(\mathbf{y}'_{(m)}) = \text{Order}(\mathbf{h}_{N_s-1}) = 2N_s. \quad (\text{A10})$$

RedAB - RedAB is similar to the RecAB since both use a recurrent module. However, RedAB only samples one order in which the outputs of RecAB $\{\mathbf{y}'_{(m)}\}_{m=0}^{N_s-1}$ get attended. Again, using the recurrent representation, we now have

$$\text{Order}(\mathbf{h}'_{(t+1)}) = \text{Order}(\mathbf{h}'_{(t)}) + \text{Order}(\mathbf{y}'_{\sigma(t+1)}) \quad (\text{A11})$$

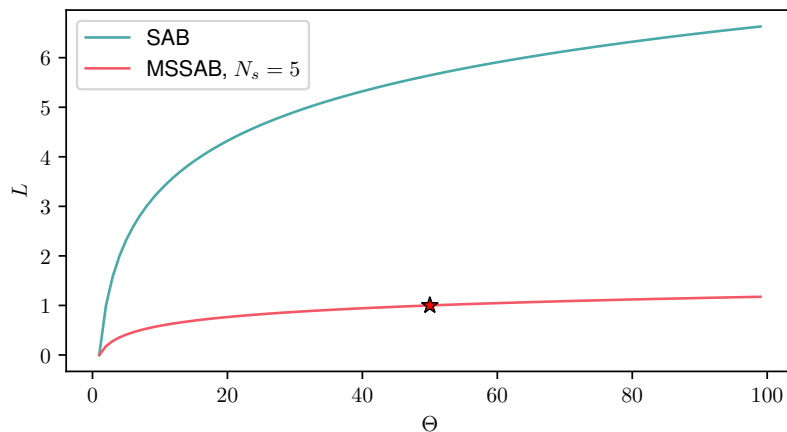
$$= \text{Order}(\mathbf{h}'_{(t)}) + 2N_s, \quad (\text{A12})$$

$$\text{Order}(\mathbf{h}'_{(0)}) = \text{Order}(\mathbf{y}_{\sigma(0)}) = 2N_s. \quad (\text{A13})$$

Unrolling the recursive relation, we obtain

$$\text{Order}(\mathbf{z}) = \text{Order}(\mathbf{h}'_{N_s-1}) = 2N_s^2. \quad (\text{A14})$$

We have shown that a single layer of MSSAB can access moments up to $2N_s^2$ -th order. By stacking L layers of MSSAB, we can reach $(2N_s^2)^L$ -th moments.



SFig. 3: Number of layers L required for SAB and MSSAB to reach moments of order Θ . We omit the ceiling ($\lceil \cdot \rceil$) operation in the plot for simplicity. For SAB, the green curve plots $L = \log_2 \Theta$. For MSSAB, we plot $L = \log_{2N_s^2} \Theta$ for $N_s = 5$ (red curve). The red star marks 1 layer of MSSAB with N_s , the setup used in our RQC training in SM section D.

Second, we consider the runtime complexity of the MSSAB versus the SAB. In a SAB, attention scores are computed between each pair of set elements, accessing up to second-order moments. Consequently, the computational complexity

scales quadratically with the input set size N , resulting in an $O(N^2)$ complexity. Our MSSAB remains a similar quadratic scaling of complexity $O(N^2)$. Therefore, accessing higher moments with fewer layers makes MSSAB more efficient than SAB.

To reach moments of order Θ , one need $L = \lceil \log_{2N_s^2} \Theta \rceil$ layers of MSSAB. In contrast, reaching the same order needs $\lceil \log_2 \Theta \rceil$. We show in SFig. 3 a scaling of the number of layers required for SAB or MSSAB to reach moments of desired order Θ . Clearly, to reach larger Θ , the number of layers needed for SAB grows much faster than MSSAB. With $L = 1$ layer of MSSAB with $N_s = 5$, we can access $\Theta = 50$, marked by a red star in SFig. 3. In contrast, we need $L = 6$ SAB layers to reach the same order $\Theta = 50$ with SAB.

4. Pooling Attention Block (PAB) Decoder

While the MSSAB encoder handles various orders of moments between bit-strings, the principal operation of the decoder is to pool out useful information from the encoder output while respecting the permutation invariance of the bit-strings. Unlike ordinary pooling operations (such as averaging/summing over snapshots), pooling attention block (PAB) enables importance-sampling by assigning weight through pooling attention score.

The decoder of QuAN consists of one layer of pooling attention block (PAB) and a final single-layer perceptron to output a single scalar value, which is the label prediction confidence. The output of the encoder \mathbf{z}_μ^α is fed into the decoder as its input. Note that, so far, the set dimension, indexed by α , has the dimensionality as the original input \mathbf{x} divided by N_s . In the decoder, the PAB performs the essential operation, which weighs different set elements differently so that elements with important features contribute more to the final result. Writing explicitly, the PAB first transforms the encoder output as

$$\begin{aligned} \mathbf{p}_\mu &= S_\mu + \sum_{\beta=1}^{N/N_s} \text{Softmax} \left[\sum_{\rho\lambda} \frac{1}{\sqrt{d_h}} \left(S_\rho K''_{\rho\lambda} \mathbf{z}_\lambda^\beta \right) \right] \sum_{\nu} V''_{\mu\nu} \mathbf{z}_\nu^\beta \\ &= \sum_{\beta} s'^\beta \left(S_\mu + \sum_{\nu} V''_{\mu\nu} \mathbf{z}_\nu^\beta \right), \end{aligned} \quad (\text{A15})$$

where a seed vector S is used as query vector of size $(1, d_h)$ for a weighted average \mathbf{z}^β over the set dimension, and K'' , V'' are key and value matrices of dimensions (d_h, d_h) . This operation plays an important role in making the output $y(\mathbf{X})$ set permutation invariant, which means the output is the same even when shuffling the set element. Moreover, the pooling attention score s'^β can be considered as a weight of \mathbf{z}^β ; therefore, \mathbf{p} can be considered as a weighted sum of encoder output. (See SM section E5 for a detailed discussion on pooling attention score in identifying topologically ordered quantum states.) Here, the pooling attention score s'^β is a vector of size N :

$$s'^\beta = \text{Softmax} \left[\sum_{\rho\lambda} \frac{1}{\sqrt{d_h}} \left(S_\rho K''_{\rho\lambda} \mathbf{z}_\lambda^\beta \right) \right]. \quad (\text{A16})$$

Similar to SAB in the encoder, we perform a layer normalization on spatial dimension and a linear layer:

$$\mathbf{p}'_\mu = \text{LayerNorm}(\mathbf{p}_\mu) \quad (\text{A17})$$

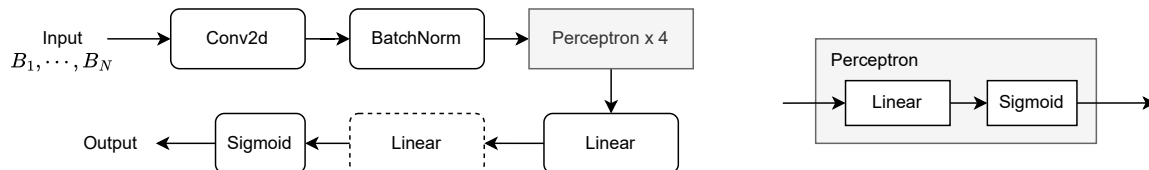
$$y(\mathbf{X}) = \text{Sigmoid} \left(\sum_{\mu} W_\mu \text{LayerNorm} [\mathbf{p}'_\mu + \text{rFF}_{\mu\nu}(\mathbf{p}'_\nu)] + b \right) \quad (\text{A18})$$

where W is a matrix of dimensions $(1, d_h)$ that converts the vector \mathbf{p}'_μ into scalar output y , which is the confidence of predicting given set \mathbf{X} into one of the classes (e.g. volume-law phase, deep circuit outcome or topological phase for the cases in the main text). S, K'', V'', W, b are learnable parameters in the decoder.

Appendix B: Comparison of QuAN and other ML architectures

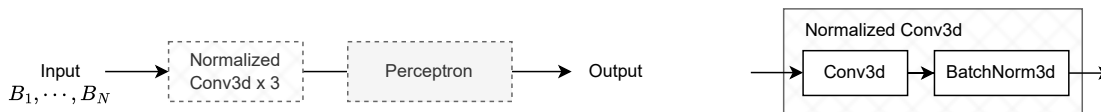
This section provides details of all the ML architectures compared with QuAN in Fig. 1(e). In particular, we highlight the main differences between these architectures and the QuAN architecture we propose in this work. The models maintain approximately the same total number of trainable parameters to make a controlled comparison between different architectures.

a. Multi-layer perceptron (MLP) - The multi-layer perceptron (MLP) model contains 4 layers of perceptrons in the encoder, followed by the decoder block composed of one linear layer and another perceptron (see SFig. 4). The first linear layer in the decoder transforms each set element independently, while the second linear layer combines information from different set elements. Note that the MLP architecture does not use the attention mechanism and also does not respect set element permutation invariance.



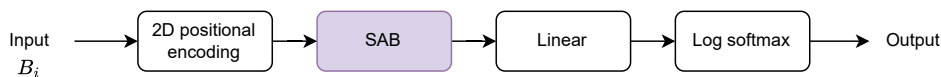
SFig. 4: Schematic MLP architecture. The inner structure of the perceptron block is shown in the right panel. The dash-lined blocks indicate inter-set-element operations. Blocks with solid lines act on each set element independently.

b. Convolutional neural network (CNN) - The convolutional neural network (CNN) architecture (see SFig. 5) treats the input data as a 3-dimensional object. Hence, it does not respect the permutation invariance of set elements either. The input 3D array goes over 3 layers of normalized 3D convolution that extracts relevant features into n_c channels, and the subsequent linear layer and sigmoid function outputs a binary classification probability.



SFig. 5: Schematic CNN architecture. The dash-lined blocks indicate inter-set-element operations. Blocks with solid lines act on each set element independently.

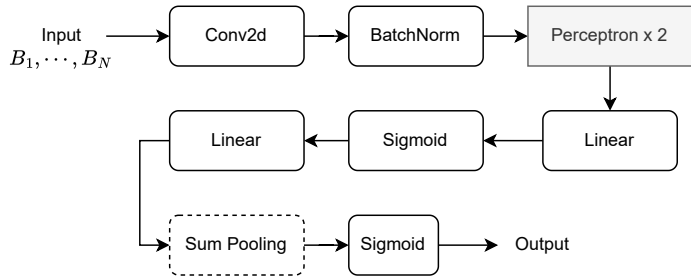
c. Transformer (Transf.) - The transformer attends to spatial correlation within one measurement outcome. In contrast to all the other models, the transformer takes one bit-string as an input at a time, considering each bit (0 or 1) as a token. The bit-string goes through a 2D positional encoding followed by ordinary self-attention blocks, a linear layer, and an activation function, as shown in SFig. 6. Compared to ordinary transformers, our *Transf.* lacks a decoder part, i.e., this model is analogous to an ordinary transformer encoder.



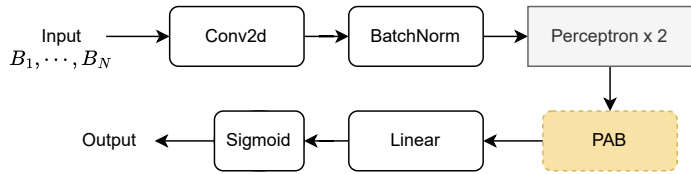
SFig. 6: Schematic transformer architecture.

d. Set multi-layer perceptron (SMLP) - The set multi-layer perceptron (SMLP) is similar to the above-mentioned MLP architecture. The main difference between MLP and SMLP lies in the decoder, shown in SFig. 7. For SMLP, we modify the decoder such that the model respects the set element permutation invariance. SMLP only contains linear layers, summation pooling, and final non-linear activation functions. The attention mechanism is absent in this model.

e. Pooling attention block (PAB) - In PAB architecture shown in SFig. 8., we replace the encoder of QuAN with two MLP layers. The decoder still contains the PAB block, which utilizes the attention mechanism.



SFig. 7: Schematic SMLP architecture. The dash-lined blocks indicate inter-set-element operations. Blocks with solid lines act on each set element independently.



SFig. 8: Schematic PAB architecture. The dash-lined blocks indicate inter-set-element operations. Blocks with solid lines act on each set element independently.

Appendix C: Driven Hard-core Bose-Hubbard model

1. Data acquisition

In this section, we provide further details of learning the entanglement transition in the driven hard-core Bose-Hubbard model.

We use the data acquired from a 4×4 array of superconducting transmon qubits as described in Ref. [4]. In this system, the on-site interaction, determined by the anharmonicity of the transmon qubits, is much stronger than the exchange interaction. Therefore, the system can be described by a Hard-core Bose-Hubbard (HCBH) Hamiltonian:

$$\hat{H}_{\text{HCBH}}/\hbar = \sum_{\langle j,k \rangle} J_{jk} \hat{\sigma}_j^+ \hat{\sigma}_k^- - \sum_j \frac{\epsilon_j}{2} \hat{\sigma}_j^z, \quad (\text{C1})$$

where $\hat{\sigma}_j^+$ ($\hat{\sigma}_j^-$) is the raising (lowering) operator for a two-level system at site j , and $\hat{\sigma}_j^z$ is the Pauli-Z operator. The first term describes the particle exchange interaction between neighboring lattice sites with strength J_{jk} , with an average strength of $J/2\pi = 5.9(4)$ MHz. The second term represents the site energies, tuned by the transmon transition frequencies with an accuracy of 300 kHz ($\approx 5 \times 10^{-2} J$) in the device [5]. This system features site-resolved, multiplexed single-shot dispersive qubit readout and enables simultaneous tomographic measurements of the qubit states when combined with single-qubit gates. In order to prepare superposition states across the energy spectrum of the lattice, the interacting qubits are simultaneously driven via a common control line. The Hamiltonian of the driven lattice is

$$\hat{H}/\hbar = \sum_{\langle j,k \rangle} J_{jk} \hat{\sigma}_j^+ \hat{\sigma}_k^- + \frac{\delta}{2} \sum_j \hat{\sigma}_j^z + \Omega \sum_j (\alpha_j \hat{\sigma}_j^- + \text{h.c.}), \quad (\text{C2})$$

where δ is the detuning between the drive and the qubit frequencies (all sites have the same energy). The drive strength Ω can be tuned by varying the amplitude of the applied drive pulse. The common drive couples to each qubit with a complex coefficient α_k (see Ref. [4] for details).

By changing the drive detuning δ , the distribution of the superposition states across the HCBH energy spectrum can be controlled: with detuning $\delta = 0$, the superposition state will be concentrated near the center of the energy band, whereas as the magnitude of δ increases, the superposition state approaches the edge of the energy band. Therefore, the drive detuning is an effective tuning knob to control the distribution of the state across the spectrum to study the entanglement scaling behavior in many-body systems.

2. Data preprocessing

The states $\rho = \rho(\delta, t)$ accessible in the emulation is parameterized by the driving detuning parameter δ and the driving time t . For each given state $\rho(\delta, t)$, we acquire a corresponding probability distribution $p(b) = \text{Tr}(\rho|b\rangle\langle b|)$ by experimentally measuring the state 10^4 times in the Z -basis. We then sample snapshots from each state's probability $p(b)$ to generate training and testing datasets. Given that the increase in detuning strength δ correlates directly with the total particle number, we selectively remove snapshots featuring a total particle number other than $n = 8$. Such an operation prevents the ML model from learning the trivial feature – the particle density. The resulting number of snapshots we keep for each state is $M_s = 4096$, each having $n = 8$ total particle number. We emulate 9 different values of δ/J , namely $\delta/J \in \{-2, -1.5, \dots, 0, \dots, 1.5, 2\}$. For each fixed value of δ/J , we take $N_c = 17$ grid points along $t \in \{1.4 \times 10^{-7}, 1.5 \times 10^{-7}, \dots, 2.9 \times 10^{-7}, 3 \times 10^{-7}\}$ seconds, all of which are in the steady state region. Since we are interested in steady states at different δ , we batch along t . Hence, for each δ we have $M = N_c \times M_s = 17 \times 4096 = 69632$ snapshots. Our device is a 4×4 array of superconducting transmon qubits, so each snapshot also has a 4×4 rectangular geometry with $N_q = 16$ binary values.

We train our model on snapshots taken from the volume-law states at $\delta/J = 0$ and from the area-law states at $\delta/J = \pm 2$. For each δ/J , we randomly choose 12 out of 17 different values of t for *training* and keep the remaining 5 for *validation*. We then randomly partition the $M_s = 4096$ snapshots from each state $\rho(\delta, t)$ into sets of size N . Half of the sets from $\delta = \pm 2$ are combined and used in training so that the total training data size remains the same for the two classes. To train QuAN as a binary classifier between the two phases, we perform supervised learning by labeling sets from $\rho(\delta/J = 0, t)$ as $\hat{y} = 0$, and $\rho(\delta/J = \pm 2, t)$ as $\hat{y} = 1$. The details of the training procedure are discussed in the next section.

After training the model, we test the model on *testing* dataset taken from the intermediate phase region $\delta/J \in \{-1.5, \dots, 0, \dots, 1.5\}$. The *testing* sets are generated by the same procedure as the *training* sets, but at different

detuning strength δ/J . We obtain average confidence \bar{y} over testing sets in predicting the volume-law phase. For $\delta/J = 0$ and $\delta/J = \pm 2$, we present the average confidence for the reserved *validation* sets.

Model hyperparameter	
Model	SMLP, PAB, QuAN ₂ , QuAN ₄
Number of mini-sets (N_s)	1
Number of MSSAB layer (L)	0~2
Number of 2×2 Conv. channel (n_c)	7~8
Attention block: Hidden spatial dimension (d_h)	16
Attention block: Number of heads (n_h)	4
Attention block: activation function for residual connection	Sigmoid
Training hyperparameter	
Optimizer	Adam ($\beta_1 = 0.9, \beta_2 = 0.999, \epsilon = 1 \times 10^{-8}$)
L2 coefficient	5×10^{-5}
Learning rate	1×10^{-4}
LR schedule	StepLR (stepsize = 200, $\gamma = 0.65$)
Epoch	500
Dataset shuffling period	10
Batchsize	80000/ N
Initialization	Default
GPU	A100 (80GB)

TABLE I: Model setting and training hyperparameters for the driven hard-core Bose-Hubbard model. We use set size of range $N = 1 \sim 256$.

	SMLP	PAB	QuAN ₂	QuAN ₄
Encoder	Conv(1, 8, 2, 1, BatchNorm) SLP(72, 48, Sigmoid) SLP(48, 16, Sigmoid)	Conv(1, 8, 2, 1, BatchNorm) SLP(72, 48, Sigmoid) SLP(48, 16, Sigmoid)	Conv(1, 8, 2, 1, BatchNorm) MSSAB*(72, 16, 4, 1)	Conv(1, 7, 2, 1, BatchNorm) MSSAB*(63, 16, 4, 1) MSSAB*(16, 16, 4, 1)
Decoder	SLP(16, 48, Sigmoid) SLP(48, 1) Sum*, Sigmoid	PAB*(16, 16, 4) SLP(16, 1, Sigmoid)	PAB*(16, 16, 4) SLP(16, 1, Sigmoid)	PAB*(16, 16, 4) SLP(16, 1, Sigmoid)

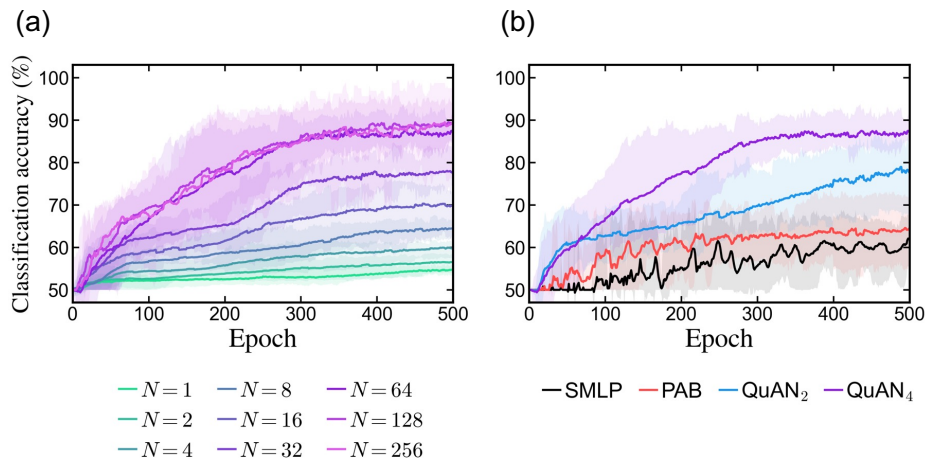
TABLE II: Architecture parameters used in models sketched in main text Fig. 2(e-g). We use data from $N_q = 16$ with 4×4 geometry for training and testing. Each layer’s arguments are as follows: Convolutional layer as Conv($n_{c,in}, n_{c,out},$ kernel, stride, normalization). Single-layer perception as SLP($d_{in}, d_{out},$ activation). MSSAB($d_{h,in}, d_{h,out}, n_h, N_s$). PAB($d_{h,in}, d_{h,out}, n_h$). The asterisk (*) denotes the module operates on a set dimension.

3. Training and testing procedure

We use PyTorch to train and test the model to discriminate volume-law and area-law entanglement scalings. Using the Adam optimization algorithm, we minimize the binary cross entropy loss function (`torch.nn.BCEloss`) of the true (actual) output and machine-predicted output of the given input set. To prevent the model from overfitting, we employ the “dataset shuffling period”; since the model input is set-structured with multiple measurement outcomes, we shuffle or regenerate the input set-structured dataset every 10 epochs to ensure the model can explore various combinations of measurement outcomes. This scheme is used throughout the paper. Training hyperparameters are listed in Table I, and parameters of architectures are listed in Table II. We train different models and set sizes (ranging from $N = 2^0 = 1$ to $N = 2^8 = 256$) independently while keeping the remaining model parameters unchanged. For each architecture, we perform 10 independent training to ensure training stability. We store the model with the highest accuracy on *validation* data. When calculating accuracies, we set the classification criteria (threshold) to be $y = 0.5$; that is, \mathbf{X}_i is classified as volume-law if the machine output is $y(\mathbf{X}_i) > 0.5$ and is classified as area-law otherwise. Comparing the machine-predicted labels for *validation* sets with the expected labels yields the validation accuracy.

We don’t know the labels in the intermediate region, where *testing* sets are generated. However, we see the phase transition from the machine confidence $y(\mathbf{X}_i)$. We get averaged confidence by averaging the machine output of confidence $y(\mathbf{X}_i)$ over testing sets. We test 10 independent models and obtain the mean and the standard error of the mean of the machine confidences.

4. Machine learning details



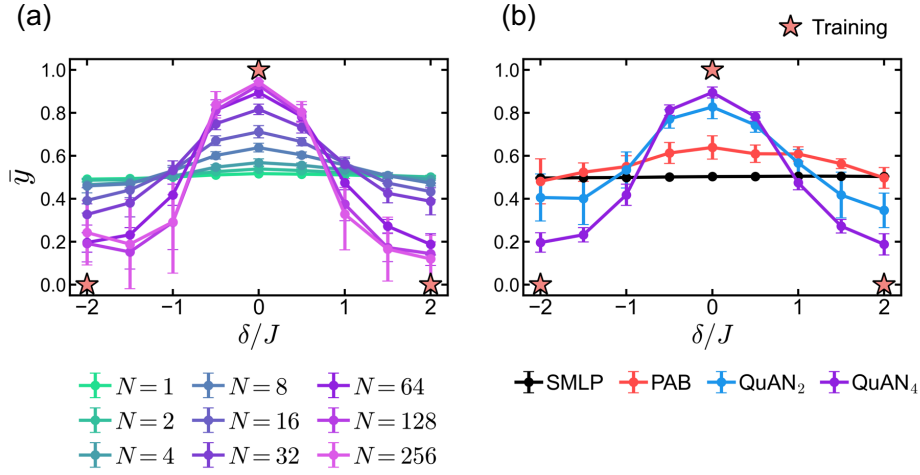
SFig. 9: Validation classification accuracy learning curves as a function of training epoch. **(a)** Validation classification accuracy curves at different set sizes N using QuAN₄. **(b)** Validation accuracy curves with different architectures (SMLP, PAB, QuAN₂ and QuAN₄) using $N = 64$. The solid line shows the mean of 10 independently trained models, and shaded regions show the minimum and maximum accuracy at each epoch.

After training, we verify the model’s performance and stability using validation accuracy as a function of epoch (see SFig. 9). Validation accuracy is determined by the percentage of correctly classified validation data points that are in either volume-law ($\delta/J = 0$) or area-law ($\delta/J = \pm 2$) state (see section C 2). For instance, an accuracy of 90% indicates that the model correctly classifies 90% of the total data. If the accuracy hovers around 50%, it suggests that the model fails to train, as random guessing would yield the same accuracy of 50% for any binary classification task.

From SFig. 9(a), we observe the differences in accuracy curves with different set sizes N we use to train QuAN₄. When the set size is small (e.g., $N < 8$), test accuracy saturates at a much lower value compared to the larger set size ($N \geq 64$). The saturated accuracy increases as we increase the set size to $N = 64$, suggesting that the model can better classify the data using larger set sizes. From the trend with increasing set size, it is clear that having a set structure for input is essential for QuAN to learn the entanglement transition. However, we observe accuracy is upper-bounded by increasing the set size beyond $N > 64$. For the two largest set sizes ($N = 128$ and 256), the accuracy is not higher than the saturated accuracy for $N = 64$. Moreover, the variance of learning curves across 10 independent training gets larger with increasing set size N due to decreased total training points. Even the set structure plays an important role; using a large set size is limited by the total number of snapshots.

SFig. 9(b) shows the accuracy curves for different architectures. All 4 models require input with a set structure, and we maintain the same set size $N = 64$ for fair comparison. Models with self-attention (QuAN₂, QuAN₄) exhibit higher accuracy saturation than models without self-attention (PAB, SMLP), which hovers around 60%. Especially, QuAN₄ accuracy saturates faster and higher compared to QuAN₂, demonstrating having more SAB layer is advantageous. Another thing to notice is that the range or variance of accuracy across 10 independent training runs (shaded region) varies among architectures. Notably, QuAN₄ demonstrates good stability with smaller variance at later epoch ≈ 500 , compared to other architectures.

Following model validation, we now test the model performance in SFig. 10 by examining the averaged confidence \bar{y} averaged over the testing dataset that includes intermediate region $\delta/J \in \{-1.5, -1.0, -0.5, 0.5, 1.0, 1.5\}$ (see also main text Fig. 2(e-g) in the main text). If the averaged confidence \bar{y} is near 0.5, we consider the model fails to distinguish volume-law and area-law features. In SFig. 10(a), we present the average confidence for predicting volume-law, using different set sizes N for our model QuAN₄. Notably, as we increase the set size to $N = 64$, the transition prediction becomes sharper, emphasizing the importance of utilizing a set structure. However, for larger set sizes beyond $N > 64$ (i.e., $N = 128$ and 256), the average confidence trend over drive detuning δ/J remains the same with the $N = 64$ training. Moreover, the variance (error bar) of average confidence \bar{y} across 10 independent training increases with set size $N > 64$, which aligns well with the accuracy curve in SFig. 9(a). Despite the benefits of large set sizes, there is a trade-off due to a fixed number of snapshots $M = 69632$; by increasing the set size, we sacrifice the total number of sets available. Specifically, we have a total $M/N = 1088$ sets for $N = 64$, $M/N = 544$ sets for $N = 128$ and $M/N = 272$ sets for $N = 256$. Beyond a set size of $N = 64$, we encounter a risk of model overfitting to the training



SFig. 10: Average confidence \bar{y} as a function of detuning δ/J . The error bar represents the standard error of averaged confidence over 10 independent training. **(a)** Average confidence by QuAN₄ with varying set sizes N . **(b)** Average confidence with different architectures (SMLP, PAB, QuAN₂ and QuAN₄) using $N = 64$. The red stars indicate the training points $\delta/J = 0, \pm 2$.

dataset if we don't use sufficient training data points. We conclude that a set size beyond $N = 64$ does not have an advantage in observing entanglement transition.

In SFig. 10(b), we present the entanglement transition witnessed with different architectures while maintaining the same set size $N = 64$. Models with self-attention (QuAN₂ and QuAN₄) exhibit a sharper distinction between area-law and volume-law phases compared to models without self-attention (PAB, SMLP). Moreover, we observe QuAN₄ achieves the smallest error bar (variance across 10 independent training) except for SMLP, which already demonstrates poor performance in observing entanglement transition. This result again highlights the advantage of QuAN₄ that can access high moments between sampled bit-strings.

5. Correlation as a witness of entanglement

A useful witness of the transition between the area-law and volume-law entangled states for the HCBH model is the correlation in the X direction. In fact, it is shown in Ref. [6] that the connected correlation function of a physical observable M between two disjoint regions A and B is upper bounded by the mutual information between these two regions:

$$(\langle M_A M_B \rangle - \langle M_A \rangle \langle M_B \rangle)^2 \leq 2 \|M_A\|^2 \|M_B\|^2 I(A : B). \quad (\text{C3})$$

Here $\|M\|$ is the norm of the operator M , and the mutual information is defined as

$$I(A : B) \equiv S_A + S_B - S_{AB}, \quad (\text{C4})$$

where S_A is the von Neumann entropy of the reduced density matrix via tracing out the region B from the density matrix ρ_{AB} of the two regions: $\rho_A = \text{Tr}_B(\rho_{AB})$, and similarly for S_B . Therefore, in an area-law entangled state where the mutual information decays exponentially, the correlation function will decay no slower than exponentially. In contrast, for the volume-law entangled state, the entanglement entropy scales with the size of each (sub)system. Therefore, the mutual information between A and B almost vanishes no matter the size or distance of A and B . Hence, the correlation function will also remain small across the distances.

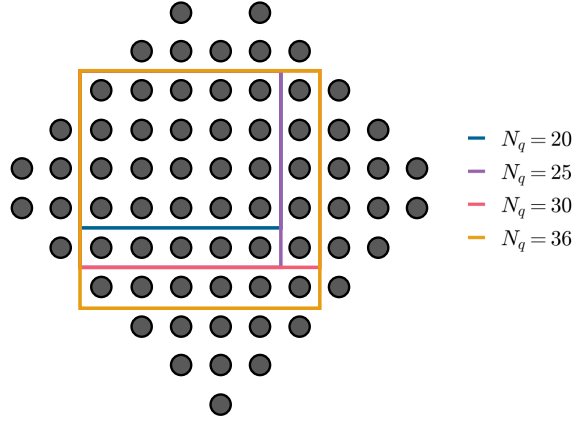
In practice, the choice of the observable M depends on the physical nature of each specific system. A suitable option for the coherent-like state obtained from the HCBH Hamiltonian would be $M = \hat{\sigma}^x$. This is mainly due to the fact that the particle exchange interaction in the Hamiltonian in Eq. (C1) happens between the spin components $\hat{\sigma}^\pm$. Indeed, as shown in Fig. 2(f,g) in Ref. [4], the connected correlation function $\langle \hat{\sigma}_i^x \hat{\sigma}_j^x \rangle - \langle \hat{\sigma}_i^x \rangle \langle \hat{\sigma}_j^x \rangle$ decays exponentially in the area-law entangled phase with a finite correlation length, while deep in the volume-law entangled phase the correlation function regardless of distance.

Appendix D: Random quantum circuit

1. Data acquisition

a. Quantum processor details and experimental procedure

The random quantum circuit experiment was conducted on a Google Sycamore processor composed of 70 frequency-tunable transmon qubits with tunable couplers. The quantum processor used has a similar design to Ref. [7] and was carried out on the same processor used in previous works, where typical coherence times, readout errors, and single and two-qubit gate errors on this particular chip can be found in Ref [8, 9]. The two-qubit gates used for this experiment are iSWAP-like gates with an iSWAP angle $\theta \approx 0.5\pi$ and conditional phase angle $\phi \approx 0.1\pi$ [9]. We collected data on rectangular subarrays of $N_q = 20, 25, 30$ and 36 qubits (see SFig. 11) with variable circuit depth $d = 4, 6, 8, 10, 12, 14, 16, 18$ and 20. For every N_q and d , we collected data on 50 different random circuit instances. Each instance contains a different sequence of single-qubit gates randomly chosen from gate set $\{\sqrt{X^{\pm 1}}, \sqrt{Y^{\pm 1}}, \sqrt{W^{\pm 1}}, \sqrt{V^{\pm 1}}\}$, with $W = (X + Y)/\sqrt{2}$ and $V = (X - Y)/\sqrt{2}$. For each of the $N_c = 50$ random circuit instances we performed $M_s = 500,000$ ($M_s = 2,000,000$) Z -basis measurements for $N_q = 20, 25, 30$ ($N_q = 36$). Thus, $N_c \times M_s$ bit strings were collected for each (N_q, d) pair.



SFig. 11: Layouts of Google Sycamore processor with 70 qubits (dark grey circles). The subarrays used for system sizes $N_q = 20, 25, 30$, and 36 are marked in colored boxes.

b. Simulation and linear cross-entropy benchmarking (XEB)

In main text Fig. 3(c,f), we show the linear cross entropy benchmark (XEB) $\mathcal{F}_{\text{XEB}}(N_q, d)$ as a function of circuit depth d for different system sizes N_q . Here, we present how we obtain the data.

Parallelized over 8 NVIDIA A100 GPUs, we can simulate up to $N_q = 36$ qubits exactly. We use Cirq [10] to simulate the same random quantum circuit instances used in the experiment. For each circuit instance, we evolve an all-zero product $|0\rangle^{\otimes N_q}$ with the circuit to get a state vector $|\psi_s(N_q, d)\rangle$, where $d \in [4, 6, \dots, 20]$ represents the depth of the circuit, and $s \in [1, 2, \dots, N_c]$ represents $N_c = 50$ different circuit instances. To simulate measuring a state in Z -basis, we sample from the distribution given by $|\langle \psi_s(N_q, d) | B_i \rangle|^2$. Similar to the sample size we have in experiments, we draw $M_s = 500,000$ samples for $N_q = 20, 25, 30$ and $M_s = 2,000,000$ for $N_q = 36$. The linear XEB is defined as,

$$\mathcal{F}_{\text{XEB}}(N_q, d, s) = 2^{N_q} \langle p(B_i) \rangle_i - 1 = 2^{N_q} \sum_{b \in (0,1)^{\otimes N_q}} p(b)^2 - 1 \quad (\text{D1})$$

where $p(B_i) = |\langle \psi_s(N_q, d) | B_i \rangle|^2$. From a finite set of samples, we can get an estimate of \mathcal{F}_{XEB} ,

$$\mathcal{F}_{\text{XEB}}(N_q, d, s) \approx 2^{N_q} \left(\frac{1}{M} \sum_{i=1}^M p(B_i) \right) - 1 \quad (\text{D2})$$

We exactly calculate simulated $\mathcal{F}_{\text{XEB}}(N_q, d, s)$ using Eq. (D1) for each state $|\psi_s(N_q, d)\rangle$, and then average over $N_c = 50$ circuit instances with the same circuit depth to get $\mathcal{F}_{\text{XEB}}(N_q, d)$ in main text Fig. 3(c). The error bar in the plot is the standard error over multiple circuit instances. For experimental XEB (see main text Fig. 3(e)), we estimate $\mathcal{F}_{\text{XEB}}(N_q, d, s)$ using Eq. (D2) for each state $|\psi_s(N_q, d)\rangle$, and then average over $N_c = 50$ circuit instances to get estimated $\mathcal{F}_{\text{XEB}}(N_q, d)$.

2. Data preprocessing

Out of $N_c = 50$ circuit instances for each depth, we randomly choose $0.7N_c = 35$ circuit instances as *training* circuits and the remaining 15 as *testing* circuits. For each $|\psi_s(N_q, d)\rangle$, we partition the M_s measurement snapshots sampled from the state into sets of set size N . For $N_q < 36$ and the set size of $N = 10,000$, we have $35 \times M_s/N = 1750$ training sets per depth d , $15 \times M_s/N = 750$ sets for testing each. For $N_q = 36$, we have 7000 training sets and 3000 testing sets. (Note that we have $M = N_c \times M_s = 50 \times 500,000 = 25,000,000$ bitstrings for $N_q < 36$ and $M = N_c \times M_s = 50 \times 2,000,000 = 100,000,000$ bitstrings for $N_q = 36$.) We combine all sets from the 35 (15) different circuit instances with the same circuit depth d and label them as the same class when generating the *training* (*testing*) dataset. We train our models on data from two depths d and 20, labeled by $\hat{y} = 0$ and $\hat{y} = 1$ correspondingly.

As a baseline, we also train the model with shallow and deep depth both at $d = 20$. In this case, we expect the model to fail the classification task and have accuracy at 50%. We randomly choose 35 circuit instances as a training circuit from $d = 20$, partition them into sets, and assign half of the sets to shallow depth (label $\hat{y} = 0$) and the other half to deep depth (label $\hat{y} = 1$). Testing datasets are constructed from the remaining 15 circuit instances in the same way.

3. Training and testing procedure

We use PyTorch to train the models as binary classifiers to distinguish shallow-depth circuit measurement outcomes from deep-depth circuit measurement outcomes. We set the reference deep to be $d = 20$ and vary the shallow depth. We use Adam optimization with binary cross-entropy loss and also utilize the dataset shuffling method, described in section C3. Detailed model and training hyperparameters are presented in Table V and IV. We employ a step learning rate scheduler and Xavier normal initialization to enhance learning further. We use the MSSAB module with $N_s = 5$ to deal with large set size $N = 10,000$. We keep the model with the highest test accuracy during each training run. The training curves are shown in SFig. 12.

Model hyperparameter	
Model	QuAN ₅₀
Number of mini-sets (N_s)	5
Number of MSSAB layer (L)	1
Number of 1×1 Conv. channel (n_c)	16
Attention block: Hidden spatial dimension (d_h)	16
Attention block: Number of heads (n_h)	4
Attention block: activation function for residual connection	ReLU
Training hyperparameter	
Optimizer	Adam($\beta_1 = 0.9, \beta_2 = 0.999, \epsilon = 1 \times 10^{-8}$)
L2 coefficient	5×10^{-5}
Learning rate	3.5×10^{-5}
LR schedule	StepLR(stepsize = 100 ~ 200, $\gamma = 0.65$)
Epoch	400
Dataset shuffle period	10
Batchsize	20
Initialization	xavier_normal
GPU	A100 (80GB)

TABLE III: Model setting and hyperparameters used to train the model with random quantum circuit data. We use set size of $N = 10000$.

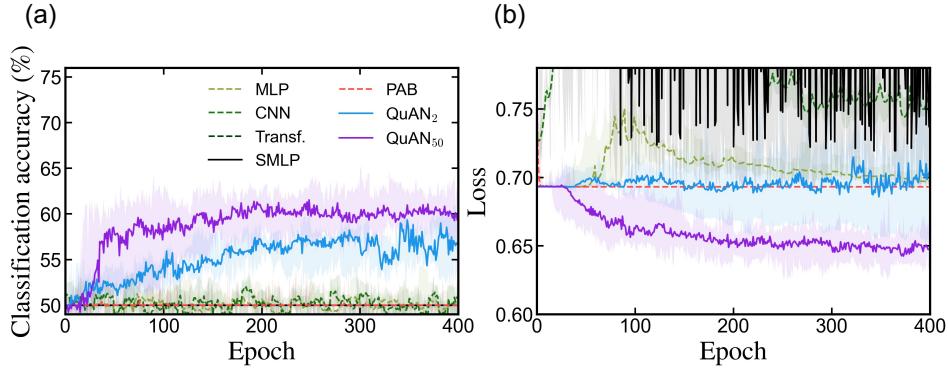
For the results presented in the main text, we perform 8 independent training runs on noiseless simulated data for each depth pair $(d, 20)$, where $d \in \{4, 6, \dots, 20\}$. Therefore, for each $(d, 20)$, we have 8 models. We then test the trained models with simulated testing data from the same depth pair $(d, 20)$. Note that this is different from the

hard-core Bose-Hubbard model (section C 3) and toric code (section E 3) studies, where we validate models trained on specific training parameter points across the entire phase space. We then calculate the mean and the standard error of the mean of the accuracy from the 8 independent models for each $(d, 20)$, as presented in the main text Fig. 3(d). We then tested the experimental data generated with Google’s Sycamore processor. For each $(d, 20)$, we apply the 8 models trained on simulated data to classify experimental data at the same depth pair (see main text Fig. 3(g)). Note that we use experimental data from the same testing circuit instances.

	MLP	CNN	Transf.
Encoder	Conv(1, 16, 2, 1, BatchNorm) SLP(256, 16, Sigmoid)	Conv3d(1, 4, (500,2,2), (50,1,1), BatchNorm) Conv3d(4, 4, (50,2,2), (5,1,1), BatchNorm)	PE2d($d = 16$) SAB(32, 16, 4)
Decoder	SLP(16, 16, Sigmoid) SLP(16, 1, Sigmoid) SLP*(N , 1, Sigmoid)	Conv3d(4, 16, (5,2,2), (1,1,1), BatchNorm) SLP(1600, 1, Sigmoid)	SLP(400, 1, log softmax)
	SMLP	PAB	QuAN
Encoder	Conv(1, 16, 2, 1, BatchNorm) SLP(256, 48, Sigmoid) SLP(48, 16, Sigmoid)	Conv(1, 16, 2, 1, BatchNorm) SLP(256, 48, Sigmoid) SLP(48, 16, Sigmoid)	Conv(1, 16, 2, 1, BatchNorm) MSSAB*(256, 16, 4, N_s)
Decoder	SLP(16, 48, Sigmoid) SLP(48, 1) Sum*, Sigmoid	PAB*(16, 16, 4) SLP(16, 1, Sigmoid)	PAB*(16, 16, 4) SLP(16, 1, Sigmoid)

TABLE IV: Detailed model architectures used in main text Fig. 3(e). We train using data from $N_q = 25$ with 5×5 geometry. Each layer’s arguments as followed: Convolutional layer as Conv($n_{c,in}$, $n_{c,out}$, kernel, stride, normalization). Single perception as SLP(d_{in} , d_{out} , activation). 2D Positional encoding as PE2d(d_h). SAB($d_{h,in}$, $d_{h,out}$, n_h) and MSSAB($d_{h,in}$, $d_{h,out}$, n_h , N_s). PAB($d_{h,in}$, $d_{h,out}$, n_h). * denotes the module operates over a set dimension.

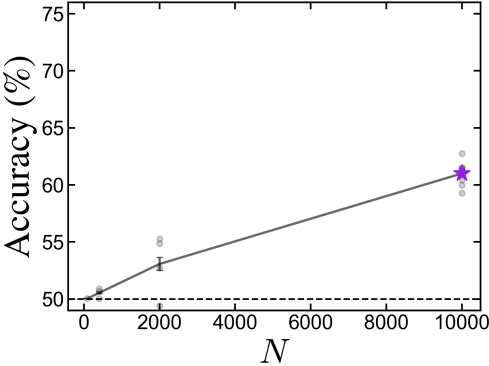
4. Machine learning details



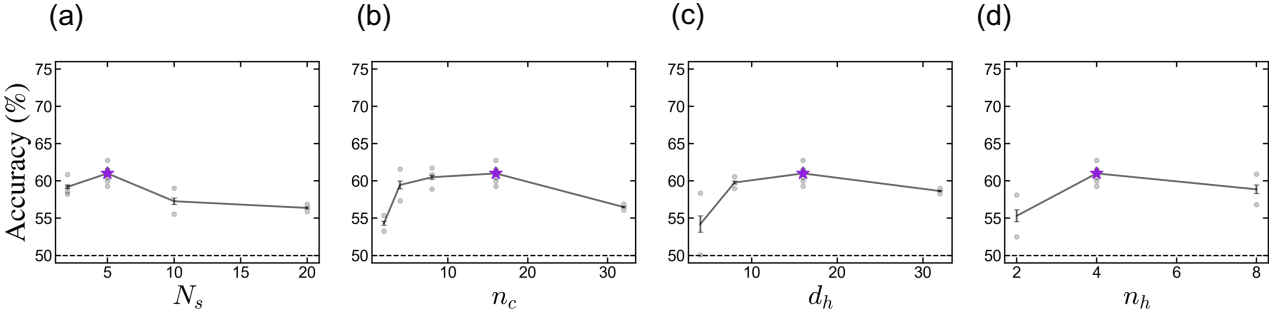
SFig. 12: **(a)** The learning curve of test classification accuracy compared at different architectures using $N = 10000$. **(b)** The learning curve of test loss compared at different architectures. We use testing data from the system size $N_q = 25$ and shallow depth $d = 8$. The solid line indicates the median of 5 independently trained models, and shaded regions show the minimum and maximum test accuracy among 5 models at each epoch.

In SFig 12, we show the learning curves to check the model’s performance and stability using test accuracy and loss curve as a function of epoch. We use simulated data from depth pair $(8, 20)$ for $N_q = 25$. The test accuracy is determined by the percentage of correctly classified test data from depths 8 and 20. Test loss is calculated through binary cross-entropy between input true label $\hat{y} = 0, 1$ and model confidence $y(\mathbf{X})$ (see section A 1). The loss function quantifies how much machine confidence deviates from the true label. The increasing test loss over epochs signals overfitting to the training dataset and poor generalization to the testing dataset. As previously discussed in the main text Fig. 3(e), only QuAN₂ and QuAN₅₀ distinguish depth 8 and 20, while other architectures (MLP, CNN, Transf., SMLP, PAB) have accuracies fluctuating near 50%. Testing loss curves for these models diverge or stay constant,

implying the model fails to distinguish between depth 8 and 20 data. Now, if we look at the accuracy curves for QuAN₂ and QuAN₅₀, we observe both accuracy curves stay higher than 50% up to epoch= 400 (see SFig. 12(a)). However, the testing loss for QuAN₂ is increasing, signaling overfitting of the training dataset, while QuAN₅₀ shows a decreasing trend in the loss function (see SFig. 12(b)). Moreover, QuAN₅₀ accuracy saturates to a higher value at an earlier epoch compared to QuAN₂ and also shows smaller variance across 5 independent training runs (shaded region). This demonstrates QuAN₅₀ has good stability with less dependence on randomness (model initialization, selection of training and testing circuit index, random seeds). We conclude QuAN₅₀ exhibits stable and high performance. From now on, we exclusively employ QuAN₅₀ for random quantum circuit depth classification tasks.



SFig. 13: Test classification accuracy of QuAN₅₀ using $N_q = 25$ and $d = 8$ and 20 , with varying set size $N = 80, 400, 2000$ and 10000 . Each gray dot represents the 5 independently trained models, and the purple star represents the optimal accuracy we use in the main text. The black solid lines with error bars represent the averaged accuracy over 5 models.

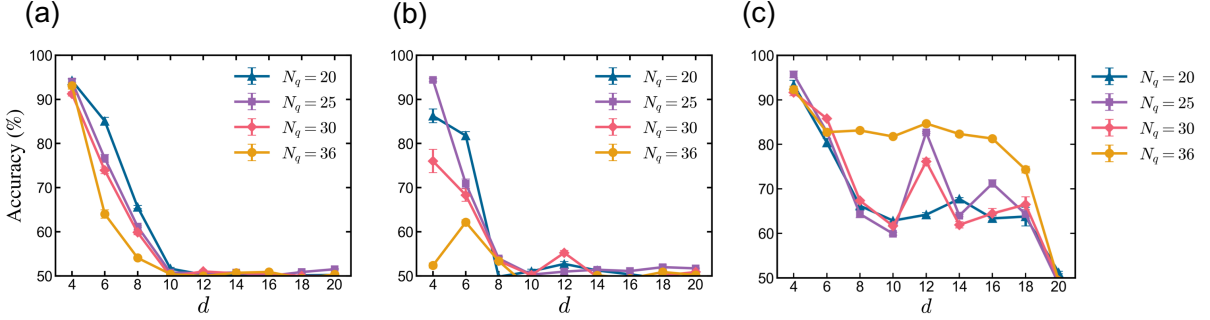


SFig. 14: Test classification accuracy of QuAN₅₀ with varying hyperparameters **(a)** number of mini-sets N_s , **(b)** number of convolutional filters n_c , **(c)** size of hidden dimension d_h , and **(d)** number of heads in multi-head attention blocks n_h . Each gray dot represents the 5 independently trained models, and the purple star represents the optimal accuracy we use in the main text. The black solid lines with error bars represent the average accuracy and standard error over 5 models.

We show in SFig. 13 the effect of varying set size N to demonstrate the importance of set structure again. We trained QuAN₅₀ with the simulated data from depth pair $(8, 20)$ for $N_q = 25$ with varying set size $N = 80, 400, 2000$ and 10000 . Validating the trained QuAN₅₀ models with test sets of the same set size as training sets, we show the test accuracy as a function of set size N (SFig. 13). Test classification accuracy increases with increasing set size, demonstrating the importance of set structure in observing the relative complexity difference between shallow and deep circuit data.

In SFig. 14, we conduct a hyperparameter study for QuAN₅₀ using the same data (depth 8 and 20 with $N_q = 25$ system with $N = 10000$, see Table V). The hyperparameters include a number of mini-sets N_s , the number of convolution channels n_c , the hidden dimension size d_h , and the number of heads n_h inside each attention block. As a baseline, we use $(N_s, n_c, d_h, n_h) = (5, 16, 16, 4)$ and tune one type of hyperparameter at a time. We record the highest testing accuracy for each training. The plots show slight changes in average accuracy with varying hyperparameters.

Therefore, we conclude that our hyperparameter choice of $(N_s, n_c, d_h, n_h) = (5, 16, 16, 4)$ yields optimal performance given current computational resource.



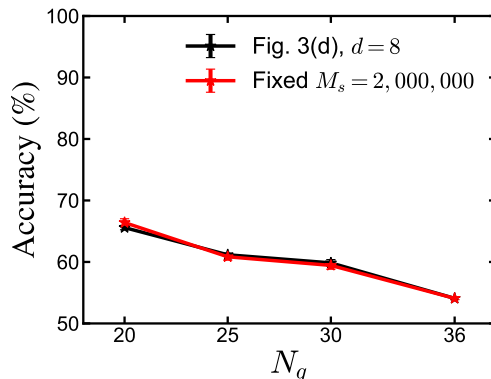
SFig. 15: **(a)** Test classification accuracy (marker) and standard error (error bar) of QuAN₅₀ trained and tested with both simulated data of N_q qubits to distinguish depth d and 20, over 8 independently trained model. **(b)** The accuracy and standard error of QuAN₅₀ trained on simulated data and tested with experimental data of depth d and 20, over 8 independently trained models. **(c)** The accuracy of QuAN₅₀ trained and tested with both experimental data averaged over 5 independently trained models.

In SFig. 15, we provide a more detailed analysis of experimental data by comparing the classification accuracy curve for simulation and experimental data. Using the model QuAN₅₀ with optimal hyperparameter setting, we train the model using the data from different (N_q, d) to learn the evolution of state complexity in random circuits as a function of depth d . Our approach involves a multiple pairwise classification task, comparing data from depth d to that from depth 20. The first classification task uses simulated data without noise, whose result is shown in main text Fig. 3(d) and SFig. 15(a). Next, we move on to classification using experimental data with noise, shown in main text Fig. 3(g) and SFig. 15(b). To inspect experimental data with QuAN, we utilize a model trained using depth d and 20 simulated data and then calculate test classification accuracy between depth d and 20 experimental data. In the main text, we highlighted that the classification accuracy for experimental data shows a similar trend to the simulated data, exhibiting a sharp transition at depth 10. However, an exception occurs for system size $N_q = 36$, where the accuracy trend differs in distinguishing depth 4 and 20. To see whether a qualitative difference exists for $(N_q, d) = (36, 4)$, we employ a new scheme of training and testing both on the experimental data while keeping all other hyperparameter settings the same (see SFig. 15(c)). We observe two key features from these curves. Firstly, QuAN readily distinguishes experimental data from depth d and depth 20. This likely reflects the increasing degree of noise that comes with circuit depth. Secondly, higher classification accuracy is seen on $N_q = 36$ data, taken on a different day from the rest ($N_q = 20, 25, 30$).

To understand how QuAN's performance varies with larger system sizes, we study the scaling of its classification accuracy with respect to system sizes (SFig. 16). We focus on distinguishing $d = 8$ and 20, which are the limits by which QuAN can differentiate between the two circuit depths. Additionally, we test on noiseless simulated bit-strings to ensure that the scaling is not influenced by noise or potential noise level dependencies with system sizes. SFig. 16 presents the scaling of QuAN₅₀'s testing accuracy with different system sizes. We examine two different training setups:

1. We train QuAN using a simulated dataset that matches the size of the experimental data. Specifically, $M_s = 5 \times 10^5$ for $N_q = 20, 25, 30$ and $M_s = 2 \times 10^6$ for $N_q = 36$. The results are shown in the black curve, which re-plots the accuracy values from the main text, Fig. 3(d), with fixed $d = 8$ at different system sizes N_q .
2. We generate additional simulation data for $N_q = 20, 25, 30$ so that all four system sizes have the same data volume, $M_s = 2 \times 10^6$. We then train QuAN₅₀ with 70% of the enlarged simulated datasets and show the testing accuracy in red. We train five independent models for each system size to obtain the average and standard error.

The two curves obtained from the slightly different training setups are consistent. Furthermore, in both setups, the accuracies exhibit sub-exponential scaling with respect to the system size.



SFig. 16: Testing classification accuracy of QuAN₅₀ trained with simulated data to distinguish simulated data of depth $d = 8$ and 20, as a function of system size N_q . (Black) We use different sample sizes for different system sizes ($M_s = 5 \times 10^5$ for $N_q = 20, 25, 30$; $M_s = 2 \times 10^6$ for $N_q = 36$) to be consistent with the experimental data volumes. Note that these accuracies are the same as taking points with different N_q but with fixed $d = 8$ in main text Fig. 3(d). (Red) Testing accuracy of QuAN₅₀ trained with 70% of $M_s = 2 \times 10^6$ bit-strings for all system sizes N_q . We train 5 independent models and show the average (markers) and standard error (error bar) of the testing accuracy.

5. Circuit depth and moments of the bitstring distribution

Although we leave it to future work to understand precisely which features of the bitstring distribution are used by QuAN to classify circuit depth, we can motivate the structure of QuAN by considering some general features of random local circuits. Specifically, permutation invariance and access to higher moments of the bitstring distribution are natural requirements of the depth classification problem.

A standard definition of the exact circuit complexity for a unitary $U \in U(2^n)$ acting on n qubits is the minimal depth (perhaps from a fixed gate set) needed to implement U exactly. In practice, we might be more interested in the approximate circuit complexity, defined analogously: given some operator norm $\|\cdot\|$, we look for the minimal depth circuit $U_{\text{circ}}(U)$ such that $\|U_{\text{circ}}(U) - U\| < \epsilon$. For random local circuits, it has been shown that the exact circuit complexity grows linearly in depth up to depths exponential in the system size [11]. Rigorous results for approximate circuit complexity are weaker [12], although it is also conjectured to grow linearly with depth [13, 14]. A fundamental question is how much can be learned about the complexity of a given unitary evolution from the experiment.

More specifically, we apply U to the initial state $|0\rangle$. The outcomes of terminal measurements in the z -basis are bitstrings $\{b_j\}$, $j \in \{1, \dots, n\}$, with probability

$$p_U(\{b_j\}) = \text{Tr} \left(|0\rangle\langle 0| U^\dagger \prod_j \frac{1 + (-1)^{b_j} z_j U}{2} U \right). \quad (\text{D3})$$

We have written (D3) in a way that emphasizes that this quantity is linear in the operator $U \otimes U^\dagger$, and k th-order products are linear in $U^{\otimes k} \otimes (U^\dagger)^{\otimes k}$. For our random circuits, the probabilities for a finite subset (not scaling with system size) of the bits equilibrate to those for infinite depth in constant depth. At the same time, there are typically an exponential number of typical bitstrings at moderate depth. This suggests that any classifier of depth would require access to additional information.

In our case, QuAN can access higher moments of the probability distribution of the bitstrings. Intuitively, as the circuit depth grows, the distribution of generated unitaries approaches the uniform (Haar) distribution over $U(2^n)$. This approach is quantified by the convergence of increasingly higher moments of the matrix entries. Explicitly, for any measure μ we define the operator $M_\mu^{(k)} = \int d\mu(U) U^{\otimes k} \otimes (U^\dagger)^{\otimes k}$. When the distance $\|M_\mu^{(k)} - M_{\mu_{\text{Haar}}}^{(k)}\| < \epsilon$, we say that μ is an ϵ -approximate k -design. The moments $M_\mu^{(k)}$ can equilibrate (at fixed precision) to the corresponding Haar moments at different depths (the relationship between k and depth is conjectured to be linear by [14], bounded by [12]), and conversely the property of being an approximate k -design implies lower bounds on the complexity [15]. The average k th order moment of the distribution of some subsets of bitstrings is just a particular matrix element of $M_\mu^{(k)}$ (see Eq. (D3)), showing that higher moments can in principle give access to depth information not available from lower ones. The XEB is an example for $k = 2$. We leave it to future work to understand what aspects of the

higher moments are learned by QuAN.

Appendix E: Toric code simulation

1. Data acquisition

We start with the Z -basis bit-string measurement from the deformed toric code state with coherent noise, now available in open source database [16] as a part of the Ref. [17]. The database includes bit-strings obtained by simulating measuring toric code deformed by coherent X, Z noise with varying strengths:

$$|\psi(g_X, g_Z)\rangle = \frac{1}{\mathcal{N}} e^{-g_X \sum_i X_i - g_Z \sum_i Z_i} |\text{TC}\rangle. \quad (\text{E1})$$

The bit-strings available in the database are simulated and sampled using projected entangled pair states (PEPS) on a 300×1000 vertex square lattice [17].

We then introduce incoherent noise through bit-flip with probability p_{flip} (see main text Eq. (6)). Thus, the resulting bit-strings are effectively sampled from mixed states $\rho(g_X, g_Z, p_{\text{flip}})$.

2. Data preprocessing

We construct training and testing datasets by transforming the Z -basis measurements of the simulated mixed-state toric code into dual lattice sites with dimensions of 300×1000 Z -plaquette terms. We extract $M_s = 8134$ snapshots for each state by slicing 300×1000 dual lattice sites into 6×6 arrays, each containing 84 qubits. These snapshots represent different quantum states, denoted as $\{\rho_s(g_X, g_Z, p_{\text{flip}})\}$, where s is index for different state. The number of distinct states corresponding to a given parameter set $(g_X, g_Z, p_{\text{flip}})$ ranges from 1 to 13. In our analysis, we fix $g_Z = 0.14$.

We create *training* and *validation* datasets at various bit-flip probability p_{flip} , in both the topological phase ($p_{\text{flip}} \in \{0, 0.005, 0.01, 0.015, 0.02\}$) and trivial phase ($p_{\text{flip}} \in \{0.3, 0.305, 0.31, 0.315, 0.32\}$). To ensure an adequate number of data points for *training*, we use different coherent noise points ($g_Z = 0.14$ and $g_X \in \{0, 0.02, 0.04, 0.06, 0.08\}$) as topological or trivial phase points (see hatched boxes in main text Fig. 4(c,d)). Importantly, we strictly sample from the region where $g_X < g_c \approx 0.22$. We have a total of $N_c = 200$ distinct states, resulting in $M = N_c \times M_s = 200 \times 8134$ snapshots per phase. Out of the 200 states, we randomly allocate $0.75N_c = 150$ states (75%) for *training* and the remaining 50 for *validation*. For a given state $\rho_s(g_X, p_{\text{flip}})$ with $M_s = 8134$ snapshots, we create a set \mathbf{X}_i of set size N by partitioning snapshots into $\lfloor M_s/N \rfloor = 127$ sets. Each snapshot within this set is composed of the same state $\{\rho_s(g_X, p_{\text{flip}})\}$. For instance, we have $150 \times \lfloor M_s/N \rfloor = 19050$ training sets, and $50 \times \lfloor M_s/N \rfloor = 6350$ *validation* sets per phase for a set size of $N = 64$.

After training the model, we test the model using *testing* dataset taken from the entire phase space of coherent noise $0 \leq g_X \leq 0.38$ and incoherent noise $0 \leq p_{\text{flip}} \leq 0.32$, which includes an intermediate region (see SFig. 17). For the points inside the training region, we randomly choose one state from the *validation* states. For the points outside of the training region, we randomly choose one state from $\{\rho_s(g_X, p_{\text{flip}})\}$. Consequently, for the set size of $N = 64$, we use $\lfloor M_s/N \rfloor = 127$ *testing* sets per each point (g_X, p_{flip}) .

3. Training and testing procedure

We use PyTorch to train and test the model to distinguish the topological and trivial phases. We again minimize the binary cross entropy loss function using Adam optimization, step learning rate scheduler, and dataset shuffling method (see SM section C3) to prevent the model from overfitting. Training hyperparameters are listed in Table III, and parameters of architectures are listed in Table VI. We train three different architectures (ranging from SMLP to QuAN₂) and different set sizes (ranging from $N = 1$ to $N = 64$) independently while keeping the remaining model parameters unchanged. For each architecture, We also perform 10 independent training to ensure stability. As listed in Table VI, we no longer use the convolution layer that inspects spatial correlation inside each snapshot. Instead, we make use of MLP as a function to deal with nonlinear correlations between closed loops within the snapshot.

During the training process, we store the model with the highest validation accuracy. This model is later used to test the dataset. We obtain a phase diagram from the machine confidence $y(\mathbf{X}_i)$; we average the machine output of confidence $y(\mathbf{X}_i)$ over 127 testing sets for each point (g_X, p_{flip}) . We calculate the averaged confidence for each of the 10 independently trained models and obtain the mean and the standard error for the averaged confidence.

Model hyperparameter	
Model	SMLP, PAB, QuAN ₂
Number of mini-sets (N_s)	1
Number of MSSAB layer (L)	0,1
Conv. channel (n_c)	No convolution
Attention block: Hidden spatial dimension (d_h)	16
Attention block: Number of heads (n_h)	4
Attention block: activation function for residual connection	ReLU
Training hyperparameter	
Optimizer	Adam($\beta_1 = 0.9, \beta_2 = 0.999, \epsilon = 1 \times 10^{-8}$)
L2 coefficient	5×10^{-5}
Learning rate	1×10^{-4}
LR schedule	StepLR(stepsize = 100, $\gamma = 0.65$)
Epoch	200
Dataset shuffle period	10
Batchsize	32768/ N
Initialization	xavier_normal
GPU	a100, 80GB

TABLE V: Model setting and hyperparameters used to train the model for toric code problem. We use set size of range $N = 1 \sim 64$.

	SMLP	PAB	QuAN ₂
Encoder	SLP(36, 48, Sigmoid)	SLP(36, 48, Sigmoid)	SLP(36, 48, Sigmoid)
	SLP(48, 16, Sigmoid)	SLP(48, 16, Sigmoid)	SLP(48, 16, Sigmoid)
Decoder	SLP(16, 48, Sigmoid)	PAB*(16, 16, 4)	MSSAB*(36, 16, 4, 1)
	SLP(48, 1)	SLP(16, 1, Sigmoid)	PAB*(16, 16, 4)
	Sum*, Sigmoid		SLP(16, 1, Sigmoid)

TABLE VI: Detailed model architectures used in main text Fig. 2(e-g). We use data from $N_q = 16$ with 4×4 geometry. (Each layer’s arguments are as follows: Convolution layer as Conv($n_{c,in}, n_{c,out},$ kernel, stride, normalization). Single perception as SLP($d_{in}, d_{out},$ activation). MSSAB($d_{h,in}, d_{h,out}, n_h, N_s$). PAB($d_{h,in}, d_{h,out}, n_h$)). * denotes the module operates on a set dimension.

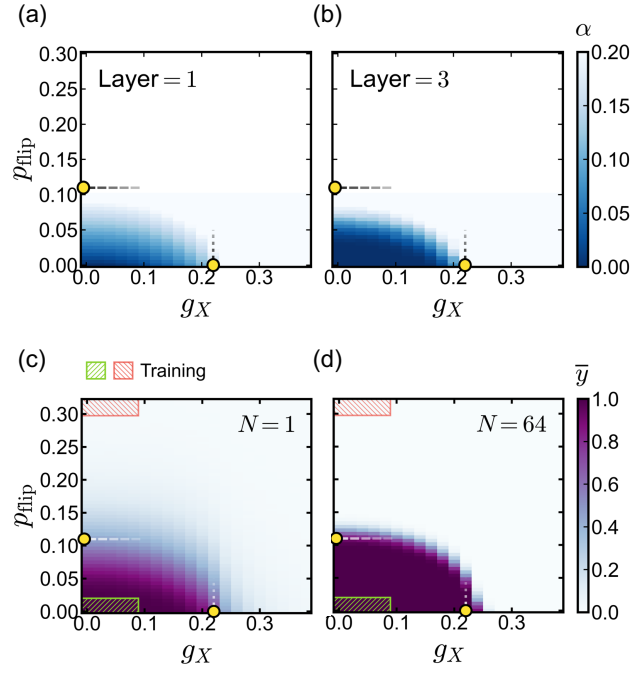
4. Benchmarking machine results

a. Benchmarking to locally error-corrected decoration (LED)

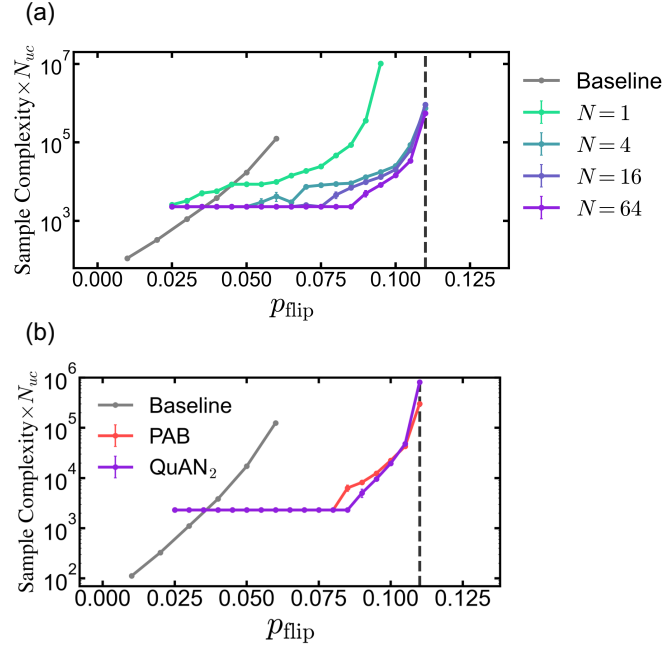
Here, we present the extended results from QuAN trained with toric code data through phase diagrams of the topologically non-trivial and trivial state, which can be constructed from average confidence $\bar{y}(g_X, p_{\text{flip}})$ as a function of coherent noise g_X and incoherent bitflip noise p_{flip} (see SFig. 17(c-d)). For comparison, we present the phase diagram obtained using “locally error-corrected decoration” (LED) (see SFig. 17(a-b), reproduced from Ref. [17]), which classifies the topological phase based on the vanishing Z -loop tension α after layers of operation. Here, the loop tension α is defined as $\langle Z_{\text{loop}}(\gamma) \rangle = e^{-\alpha|\gamma|}$ for a loop γ . As discussed in the main text, we observe that QuAN₂ sharpens the transition and even saturates the known threshold $p_c \approx 0.11$ with increasing set size N .

We quantify sample complexity as another method to benchmark model performance against LED, shown in SFig. 18. In our context, sample complexity is defined as the number of samples (snapshots) required to confirm that the state is in the topological phase with 95% confidence. We aim to evaluate sample complexity as a function of p_{flip} along $g_X = 0$ and see how the required number of samples grows as we increase the incoherent noise level. We utilize 13 different states for each $(g_X, p_{\text{flip}}) = (0, p_{\text{flip}})$ where $0.025 \leq p_{\text{flip}} \leq 0.3$, having a total $13 \times 127 = 1651$ testing sets per point. To ensure a fair comparison, we exclude points that overlap with the training points.

To determine the sample complexity at a given point, we employ a t-test between the model outputs from each set $y(\mathbf{X}_i)$ and the classification threshold at $y = 0.5$. For each model, we first randomly sample D sets out of 1651 sets from each p_{flip} , then feed in to obtain $y(\mathbf{X}_i)$, where i runs from 1 to D . (We randomly feed each set into one stored model out of 10 independently trained models with equal probability.) We conduct the t-test with the null hypothesis that “those D sets are in trivial phase with an average confidence $\bar{y} \leq 0.5$ ”. Suppose the resulting p-value (probability of observing those outputs assuming trivial phase) is less than 5%. We reject the null hypothesis in that



SFig. 17: **(a,b)** Phase diagrams of the toric code state with both coherent noise (transverse field strength g_X with fixed $g_Z = 0.14$) and incoherent noise p_{flip} as a function of Z -loop tension α using **(a)** 1 layer and **(b)** 3 layers of locally error-corrected decoration (LED) [17]. Yellow circles with vanishing dashed lines represent the known thresholds at $p_c \approx 0.11$ and $g_c \approx 0.22$. **(c,d)** Phase diagram constructed using averaged confidence \bar{y} by QuAN₂, presented in the main text Fig. 4(c,d). The hatched regions mark the training data ranges.

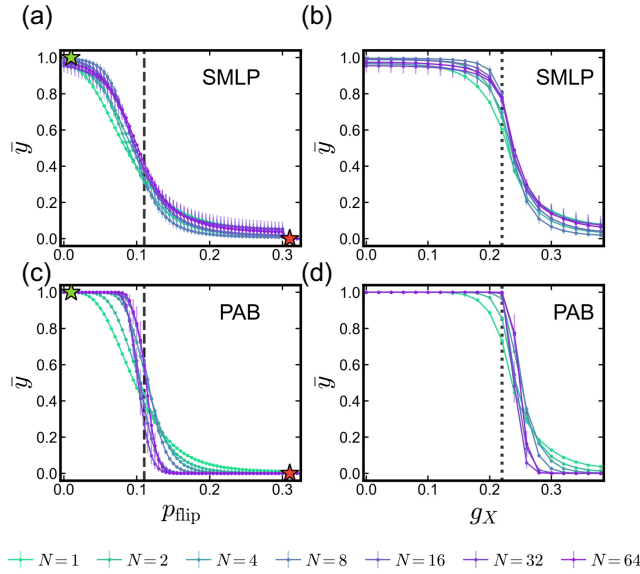


SFig. 18: Sample complexity of **(a)** QuAN₂ with varying set size N and **(b)** PAB and QuAN₂ with set size $N = 64$, using data from different p_{flip} along the $g_X = 0$ axis. $N_{uc} = 36$ is the number of unit cells in snapshots. We use sample complexity of $\langle Z_{\text{closed}} \rangle$ as the *baseline* (marked in gray) [17]. Sample complexity beyond the threshold (dashed line) is not defined.

case, indicating that the state is in the topological phase with over 95% confidence. We decrease the number of sets D , and D^* is identified as the point where the prediction fails to meet the 95% confidence level. We define $D^* \times N$ as the sample complexity, where N is the size of each set. This process is repeated 10 times to ensure the stability of our calculation, and the mean and standard error of $D^* \times N \times N_{uc}$ is plotted.

Upon obtaining sample complexities using different set sizes N and architectures (PAB, QuAN₂), we compare them with the sample complexity using bare Wilson loop $\langle Z_{\text{closed}} \rangle$ without LED [17] as a *baseline*. Here, sample complexity refers to the number of samples required to confirm $\langle Z_{\text{closed}} \rangle$ is non-zero with 95% confidence, calculated by $(2\sigma/\langle Z_{\text{closed}} \rangle)^2$ assuming Gaussian distribution of loop expectation values. In SFig. 18, we present the sample complexity at various p_{flip} using models with different hyperparameters. For QuAN₂ with varying set sizes, we observe that the sample complexity increases exponentially starting at low p_{flip} , for small set sizes (e.g., $N = 1$). However, with larger set sizes (e.g., $N = 64$), sample complexity remains relatively unchanged from its minimum value ($D^* \times N \times N_{uc} = 1 \times 64 \times 36 = 2304$) until p_{flip} approaches phase transition. Comparing this to the *baseline* (marked in grey in SFig. 18), the advantage of using QuAN₂ is clear, especially with a large set size ($N = 64$). Although the *baseline* sample complexity is lower for $p_{\text{flip}} < 0.035$, the sample complexity for QuAN₂ with $N = 64$ remains constant even until $p_{\text{flip}} < 0.09$. We hence conclude that QuAN₂ is a scalable method for a broader range of incoherent noise. The sample complexity performance of PAB trends is similar to QuAN₂ (see SFig. 18(b)), where both QuAN₂ and PAB show constant sample complexities on a broader range of incoherent noise. This indicates that PAB operation plays a central role in maintaining a low sample complexity level.

b. Benchmarking to SMLP

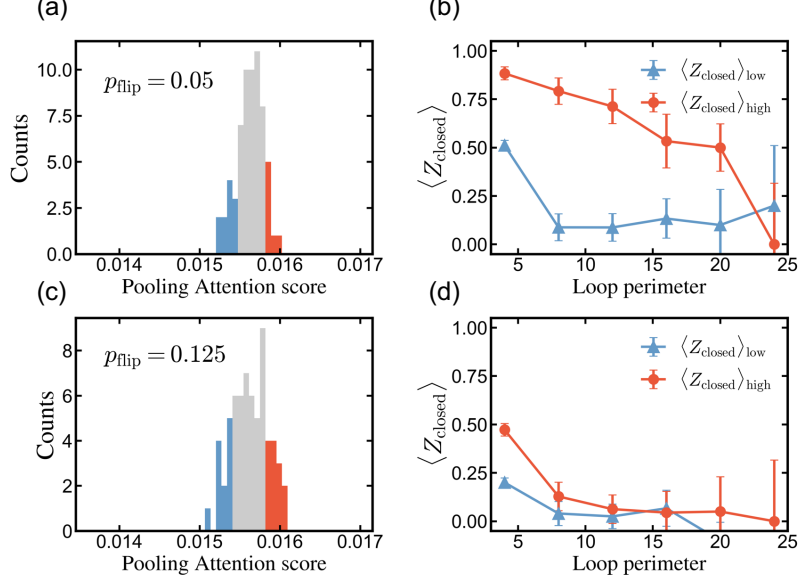


SFig. 19: **(a)** Average confidence \bar{y} (marker) and its standard error over 10 independent training (error bar) by SMLP with varying set sizes N , along the axis $g_X = 0$ with different incoherent noise rates p_{flip} . Green and pink stars represent the training points. **(b)** Average confidence \bar{y} by SMLP with varying set sizes N , along the axis $p_{\text{flip}} = 0$ with different coherent noise strength g_X . **(c)** Average confidence \bar{y} by PAB with varying set sizes N , along the axis $g_X = 0$ with different incoherent noise rates p_{flip} . **(d)** Average confidence \bar{y} by PAB with varying set sizes N , along the axis $p_{\text{flip}} = 0$ with different coherent noise strength g_X .

Now, we benchmark QuAN and PAB training to the simplest set-structured model, SMLP (see SFig. 19). To see how the characterization of the topological phase changes as we tune the architecture complexity and set size, we train three different architectures (SMLP, PAB, QuAN₂, see Table VI) with varying set sizes. In the main text Fig. 4(e-h), we made a comparison between QuAN₂ of various set sizes with SMLP ($N = 64$) and PAB ($N = 64$). Here, we would also like to show the effects of set sizes on SMLP and PAB and make a comprehensive comparison with QuAN. We draw the following two important conclusions from SFig. 19. First, for both $g_X = 0$ and p_{flip} axis, we find that SMLP prediction remains unchanged with increasing set size and even introducing a larger error bar due to a decrease in total training data points. In contrast, PAB/QuAN sharpens the phase boundary with increasing set size (see

also main text Fig. 4(e-h) for QuAN results). This implies that even with a set structure, treating every snapshot equally by averaging over snapshots does not help to predict the topological phase. Comparison of the performances between PAB and QuAN₂ leads us to a crucial conclusion: the PAB module plays a pivotal role in characterizing topological order. In the next section E5, we will make a comprehensive analysis of the PAB module, providing a deep understanding of its role in mixed-state toric code.

5. Machine analysis: PAB as an importance-sampler



SFig. 20: **(a,c)** Pooling attention score histogram from **(a)** topological state with $(g_X, p_{\text{flip}}) = (0, 0.05)$ (see main text Fig. 4(i)) and **(c)** trivial state with $(g_X, p_{\text{flip}}) = (0, 0.125)$. **(b,d)** Loop expectation value $\langle Z_{\text{closed}} \rangle$ (marker) and its standard error (error bar) as a function of the loop perimeter with high and low attention score in **(b)** topological $(g_X, p_{\text{flip}}) = (0, 0.05)$ (see main text Fig. 4(j)) and **(d)** trivial state $(g_X, p_{\text{flip}}) = (0, 0.125)$.

Here, we analyze the PAB module in more detail (see Fig. 4(i,j) in the main text) and discuss the mechanism of the PAB in predicting the topological phase. According to Eq. ((A15)-(A18)), the pooling attention output is given by

$$\mathbb{P}_\mu = \sum_\beta s'^\beta \left(S_\mu + \sum_\nu V'_{\mu\nu} \mathbf{z}_\nu^\beta \right) = \sum_\beta s'^\beta \mathbf{z}'_\mu^\beta \quad \text{with} \quad s'^\beta = \text{Softmax} \left[\sum_{\rho\lambda} \frac{1}{\sqrt{d_h}} \left(S_\rho K'_{\rho\lambda} \mathbf{z}_\lambda^\beta \right) \right], \quad (\text{E2})$$

where s'^β is the pooling attention score calculated from the encoder output \mathbf{z}^β with set index β .

Model training/testing hyperparameter	
Model	PAB
Training set size (N)	32
Model index out of 10	3
Attention block: Head index	3
Testing data details	
Testing set size (N)	64
Data points (g_X, p_{flip})	(0, 0.05) (0, 0.125)
Set number index (i)	116 43

TABLE VII: Model hyperparameters and testing data details used in SFig. 20.

First, we demonstrate the attention score's relation to Z -loop tension, which serves as the order parameter of the topological phase. To this end, we plot the histogram of pooling attention scores. Table VII shows the detailed

hyperparameters used to obtain SFig. 20(a,c). After obtaining the pooling attention score distribution for each set, we sample the highest 10 ($\sim 15\%$) and lowest 10 attention scores s'^{β} and corresponding snapshots $\{B_{\beta}|s'^{\beta} \geq s_{\text{high}}\}$ and $\{B_{\beta}|s'^{\beta} \leq s_{\text{low}}\}$. For each snapshot B_{β} with 36 Z -plaquette values, we calculate loop expectation value $\langle Z_{\text{closed}} \rangle$ at different loop perimeter $4L = 4, 8, 12, 16, 20, 24$ by multiplying Z -plaquettes inside the loop. SFig. 20(b,d) shows the mean and the standard error of the mean of loop expectation value $\langle Z_{\text{closed}} \rangle$. The mean and standard error is over 10 high (low) attention score snapshots. For snapshots in the topological phase, PAB assigns a high attention score on the snapshots with vanishing loop tensions. The lower the loop tension, the higher the attention score is assigned to the snapshot. Since the module conducts weighted sum over set index β where weight is the attention score, PAB acts as an automated importance sampler within a given set \mathbb{X}_i .

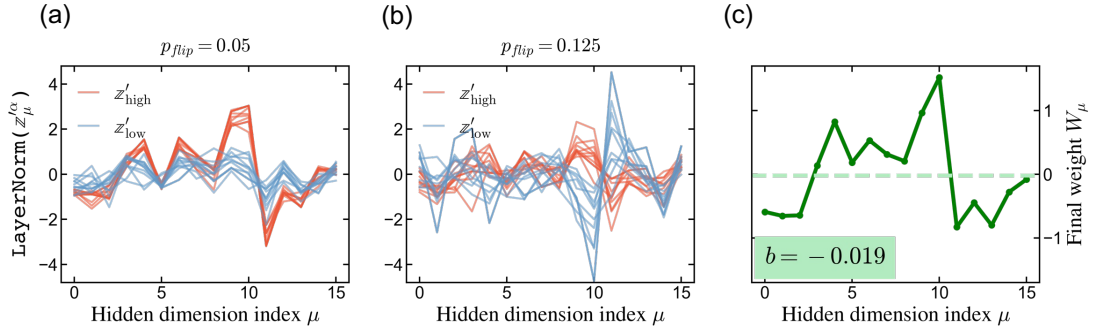
We then analyze how PAB makes a decision in testing. After Eq. (E2), the output is obtained through layer normalization, residual connection, and single-layer perception:

$$\mathbf{p}'_{\mu} = \text{LayerNorm}\left(\sum_{\beta} s'^{\beta} \mathbf{z}'_{\mu}{}^{\beta}\right) \quad (\text{E3})$$

$$y(\mathbb{X}) = \text{Sigmoid}\left(\sum_{\mu} W_{\mu} \text{LayerNorm}\left[\mathbf{p}'_{\mu} + \text{rFF}_{\mu\nu}(\mathbf{p}'_{\nu})\right] + b\right). \quad (\text{E4})$$

where $\mathbf{z} = \text{Encoder}(\mathbf{x})$, and **Encoder** is a MLP for PAB model. To simplify the process, we will compare between $\mathbf{z}'_{\mu}{}^{\beta}$ -vector and W_{μ} -vector, ignoring latter **LayerNorm** and residual layer which gives a minor shift in $\mathbf{z}'_{\mu}{}^{\beta}$. SFig. 21 compares normalized encoder output from high (low) attention score snapshots (from SFig. 20) with the final layer weight matrix.

We notice that $\mathbf{z}'_{\mu}{}^{\beta}$ -vector for high and attention score snapshots are parallel to the W_{μ} -vector. Meanwhile, $\mathbf{z}'_{\mu}{}^{\beta}$ -vector from low attention score in trivial phase is anti-parallel to the W_{μ} -vector. This final **Sigmoid** activation function then determines the output $y(\mathbb{X}_i)$: if the inner product between the importance-sampled encoder output $\mathbf{z}'_{\mu}{}^{\beta}$ and weight vector W_{μ} is positive (negative), it gives the final output of topological phase $y > 0.5$ (trivial phase $y < 0.5$). When the snapshots with high loop expectation values and high attention scores are no longer dominant, the weighted average of encoder output becomes anti-parallel with the final weight vector, and the machine prediction is no longer ‘topological.’



SFig. 21: **(a,b)** Encoder output vector \mathbf{z} for snapshots from high (red) and low (blue) attention score in **(a)** topological ($g_X, p_{\text{flip}} = (0, 0.05)$) and **(b)** trivial state ($g_X, p_{\text{flip}} = (0, 0.125)$). **(c)** The final weight W_{μ} in final perception before machine output (see Eq. (E4)) shows a similar shape compared to the encoder output vector with a high attention score. The dashed line represents the value of bias b .

-
- [1] A. Vaswani, N. Shazeer, N. Parmar, J. Uszkoreit, L. Jones, A. N. Gomez, L. Kaiser, and I. Polosukhin, Attention is all you need, *Advances in neural information processing systems* **30** (2017).
- [2] M. Zaheer, S. Kottur, S. Ravanbakhsh, B. Póczos, R. R. Salakhutdinov, and A. J. Smola, Deep sets, *Advances in neural information processing systems* **30** (2017).
- [3] J. Lee, Y. Lee, J. Kim, A. Kosiorek, S. Choi, and Y. W. Teh, Set transformer: A framework for attention-based permutation-invariant neural networks, in *International conference on machine learning* (PMLR, 2019) pp. 3744–3753.
- [4] A. H. Karamlou, I. T. Rosen, S. E. Muschinske, C. N. Barrett, A. Di Paolo, L. Ding, P. M. Harrington, M. Hays, R. Das, D. K. Kim, B. M. Niedzielski, M. Schuldt, K. Serniak, M. E. Schwartz, J. L. Yoder, S. Gustavsson, Y. Yanay, J. A. Grover, and W. D. Oliver, Probing entanglement in a 2D hard-core Bose–Hubbard lattice, *Nature* 10.1038/s41586-024-07325-z (2024).
- [5] C. N. Barrett, A. H. Karamlou, S. E. Muschinske, I. T. Rosen, J. Braumüller, R. Das, D. K. Kim, B. M. Niedzielski, M. Schuldt, K. Serniak, M. E. Schwartz, J. L. Yoder, T. P. Orlando, S. Gustavsson, J. A. Grover, and W. D. Oliver, Learning-based calibration of flux crosstalk in transmon qubit arrays, *Phys. Rev. Appl.* **20**, 024070 (2023).
- [6] M. M. Wolf, F. Verstraete, M. B. Hastings, and J. I. Cirac, Area laws in quantum systems: Mutual information and correlations, *Phys. Rev. Lett.* **100**, 070502 (2008).
- [7] F. Arute, K. Arya, R. Babbush, D. Bacon, J. C. Bardin, R. Barends, R. Biswas, S. Boixo, F. G. S. L. Brandao, D. A. Buell, B. Burkett, Y. Chen, Z. Chen, B. Chiaro, R. Collins, W. Courtney, A. Dunsworth, E. Farhi, B. Foxen, A. Fowler, C. Gidney, M. Giustina, R. Graff, K. Guerin, S. Habegger, M. P. Harrigan, M. J. Hartmann, A. Ho, M. Hoffmann, T. Huang, T. S. Humble, S. V. Isakov, E. Jeffrey, Z. Jiang, D. Kafri, K. Kechedzhi, J. Kelly, P. V. Klimov, S. Knysh, A. Korotkov, F. Kostritsa, D. Landhuis, M. Lindmark, E. Lucero, D. Lyakh, S. Mandrà, J. R. McClean, M. McEwen, A. Megrant, X. Mi, K. Michielsen, M. Mohseni, J. Mutus, O. Naaman, M. Neeley, C. Neill, M. Y. Niu, E. Ostby, A. Petukhov, J. C. Platt, C. Quintana, E. G. Rieffel, P. Roushan, N. C. Rubin, D. Sank, K. J. Satzinger, V. Smelyanskiy, K. J. Sung, M. D. Trevithick, A. Vainsencher, B. Villalonga, T. White, Z. J. Yao, P. Yeh, A. Zalcman, H. Neven, and J. M. Martinis, Quantum supremacy using a programmable superconducting processor, *Nature* **574**, 505 (2019), number: 7779 Publisher: Nature Publishing Group.
- [8] J. Hoke, M. Ippoliti, E. Rosenberg, D. Abanin, R. Acharya, T. Andersen, M. Ansmann, F. Arute, K. Arya, A. Asfaw, *et al.*, Measurement-induced entanglement and teleportation on a noisy quantum processor, *Nature* **622**, 481 (2023).
- [9] A. Morvan, B. Villalonga, X. Mi, S. Mandrà, A. Bengtsson, P. Klimov, Z. Chen, S. Hong, C. Erickson, I. Drozdov, *et al.*, Phase transition in random circuit sampling, arXiv preprint arXiv:2304.11119 (2023).
- [10] C. Developers, Cirq (2023).
- [11] J. Haferkamp, P. Faist, N. B. T. Kothakonda, J. Eisert, and N. Younger Halpern, Linear growth of quantum circuit complexity, *Nature Physics* **18**, 528 (2022).
- [12] J. Haferkamp, Random quantum circuits are approximate unitary t -designs in depth $O(n^{5+o(1)})$, *Quantum* **6**, 795 (2022).
- [13] A. R. Brown and L. Susskind, The Second Law of Quantum Complexity, *Physical Review D* **97**, 086015 (2018), arXiv:1701.01107 [gr-qc, physics:hep-th, physics:quant-ph].
- [14] F. G. S. L. Brandao, A. W. Harrow, and M. Horodecki, Local random quantum circuits are approximate polynomial-designs, *Communications in Mathematical Physics* **346**, 397 (2016), arXiv:1208.0692 [quant-ph].
- [15] F. G. Brandão, W. Chemissany, N. Hunter-Jones, R. Kueng, and J. Preskill, Models of Quantum Complexity Growth, *PRX Quantum* **2**, 030316 (2021), publisher: American Physical Society.
- [16] N. Maskara, Enhancing detection of topological order by local error correction.
- [17] I. Cong, N. Maskara, M. C. Tran, H. Pichler, G. Semeghini, S. F. Yelin, S. Choi, and M. D. Lukin, Enhancing detection of topological order by local error correction, *Nature Communications* **15**, 1527 (2024).